Computers and Geotechnics 63 (2015) 183–198

Contents lists available at ScienceDirect

Computers and Geotechnics

journal homepage: www.elsevier.com/locate/compgeo

Analysis of cohesive cracking in saturated porous media using an extrinsically enriched EFG method

Mohsen Goudarzi, Soheil Mohammadi *

School of Civil Engineering, University of Tehran, Tehran, Iran

ARTICLE INFO

Article history:
Received 25 February 2014
Received in revised form 18 August 2014
Accepted 13 September 2014

Keywords:
Mesh-free EFG method
Cohesive crack
Porous media
PU enrichment
Crack propagation
Mixed mode

ABSTRACT

The subject of this study is to investigate propagation of cohesive cracks under various mixed mode conditions in saturated porous media. The mesh-free EFG algorithm, which uses the MLS shape functions for approximating both displacement and pressure fields, is used. An enrichment approach similar to XFEM, which exploits the Heaviside step function as the enrichment function for representing the crack surfaces is adopted. Basic formulations are developed for saturated fully coupled porous media, and a series of benchmark problems are assessed through the enriched EFG formulations. Both cases of uncoupled and fully coupled formulations for the solid displacements and the water pressure are presented. For the fully coupled case, the effect of mass exchange through the fracture and the surrounding undamaged media is examined. The results predicted by the present numerical framework are in good agreement with existing solutions in the literature.

1. Introduction

Cohesive crack analysis has been the subject of extensive research topics in the past few years. It is well known that in quasi-brittle materials such as concrete and soil, instead of a highly singular stress field at the tip of fracture, the stress state can be better represented by a redistributed field in a finite region, known as the cohesive zone. Basic cohesive zone models have been introduced by Dugdale [1], Barenblatt [2] and Hillerborg et al. [3], in which a traction-separation law governs the mechanical load exchanging across the crack faces and the cohesive zone is lumped into a zero-thickness surface [4] or sometimes a finite width band [5]. These models have been extensively applied in the context of standard finite element solutions, where a conforming and highly refined mesh along the discontinuity lines is usually needed and re-meshing processes are inevitable [6].

Introduction of the extended finite element method by Belytschko and Black [7] and Moes et al. [8], based on the early contributions on the generalized finite element method [9,10] eased the re-meshing burden of the standard finite element solutions and proved to be a reliable method for modeling discrete fractures [11–18] and weak discontinuities [19–21].

Mechanics of porous-like materials were originated from the fundamental contributions by Terzaghi [22] and Biot [23], and has been the subject of vast number of studies which have resulted in the current generalized form of the governing equations based on different inherent properties of multi-phase porous systems [24–29]. Nevertheless, introduction of discontinuities in porous materials seems to be of great importance and complexity, as in different engineering applications, porous-like materials such as soil, concrete and rock are widely encountered to severe external loadings that may result in various forms of cracking and failure. Both singular and cohesive zone models have been adopted in the literature to govern the mechanical behavior of the defects in porous media. Boone and Ingraffea [30] analyzed the hydraulic fracture phenomena in fully saturated media by adopting a finite difference strategy for the water flow inside the fracture. An adaptive refinement technique for porous materials with cohesive cracks was introduced by Schrefler et al. [31] and a mathematical model for introducing cohesive fractures in porous materials was proposed in [32] using the finite element method with continuous re-meshing strategies along with the propagating fractures. Zero-thickness cohesive interface elements in the framework of the finite element method were applied to saturated porous material in Segura and Carol [33] and Lobao et al. [34]. An extension of cohesive fracture phenomena to dynamic situations was recently developed by Khoei et al. [35].

Based on the PU enrichment strategies of the basic finite element solution, Rethore et al. developed a two-scale algorithm applied to singular [36] and cohesive cracks [37]. In their works, water pressure was assumed continuous across the fracture width,

* Corresponding author.
E-mail address: smoham@ut.ac.ir (S. Mohammadi).

http://dx.doi.org/10.1016/j.compgeo.2014.09.007
0266-352X/

while due to the effect of fluid exchange between the fracture and surrounding porous media, normal gradients of water pressure were modeled as discontinuous fields with the help of distance enrichment functions. Extension of the same idea to three-phase and large deformation analysis were performed in [38,39], respectively.

Alternatively, mesh-free methods are powerful numerical tools that have been exploited widely along with the finite element method for solving general partial differential equations [40–46]. It is believed that the mesh-free methods can be superior to the finite element method in dealing with distorted meshes and general propagation problems [47,48]. Moreover, due to higher order of continuity of unknown variables, more precise and smooth stress fields are attainable [49].

Similarly, within the context of the isogeometric analysis (IGA) of poroelasticity problems, reference [50] illustrated that the higher order of continuity could validate the local mass balance unlike the usual FEM. As a result, it led to low oscillated results with even smaller time steps than the critical time step. This property eliminated the implementation of additional tip elements for cohesive fractures, where the state of crack propagation could mainly be defined by the values of stresses at the tip of fracture.

In this paper, the well-known element-free Galerkin (EFG) approach [51,52] is adopted for arbitrary modeling of cohesive crack propagation based on the extrinsic enrichment of the basic EFG solution [49,53–60]. Fully saturated porous media under external mechanical loadings within the small deformation regime are considered. Fractures are assumed to act as cohesive cracks with considerable permeabilities which allow for the water phase to flow inside. Basic governing equations are discretized for a fully coupled saturated state using the enriched MLS shape functions and different coupled/uncoupled fracturing problems of mode I and mixed mode porous materials are addressed. In the case of permeable defect, the exchange of fluid flow across the crack width is considered based on the two-scale algorithm proposed in [37]. Through the various numerical tests on dry and saturated porous materials, it is shown that the results of the present extended element-free Galerkin (XEFG) approach are in good agreement with the existing reference solutions.

2. Governing equations for fully coupled saturated porous media

In this section, the governing equations for a saturated porous medium, typically shown in Fig. 1, under the assumption of small deformation regime are presented. Convective terms are dropped out from the equilibrium equations and the formulations are developed for quasi-static situations with no inertia terms involved. Saturated porous media under the isothermal condition are assumed.

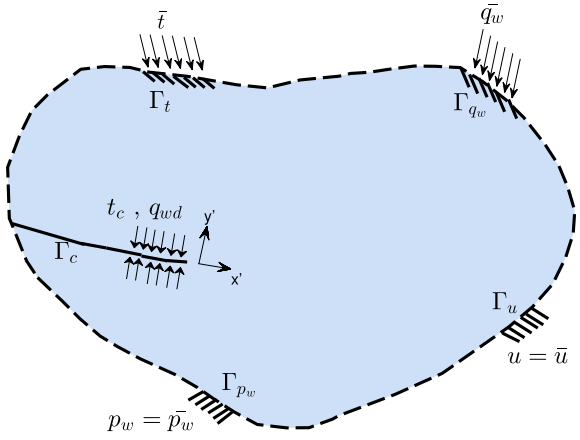

Fig. 1. An arbitrary saturated cracked domain.

The momentum balance equation for a porous medium can be written as:

$$\nabla \cdot \boldsymbol{\sigma} + \rho \mathbf{b} = 0 \tag{1}$$

where $\mathbf{b}$ is the body force and ρ is the density of the system defined as,

$$\rho = (1-n)\rho_s + n\rho_w \tag{2}$$

ρ_s and ρ_w are the density of solid and water phases and n denotes the porosity. The total stress vector $\boldsymbol{\sigma}$ can be written in terms of the effective stress vector $\boldsymbol{\sigma}''$,

$$\boldsymbol{\sigma} = \boldsymbol{\sigma}'' - \alpha \mathbf{m}(p_w) \tag{3}$$

and the constitutive relation is defined in terms of the effective stress and strain increments,

$$d\boldsymbol{\sigma}'' = \mathbf{D}(d\boldsymbol{\epsilon}). \tag{4}$$

where $\mathbf{D}$ is the elastic stiffness tensor and α is the Biot's constant,

$$\alpha = 1 - \frac{K_T}{K_s} \tag{5}$$

with K_T and K_s defined as the bulk modulus of porous skeleton and solid grains, respectively. The momentum balance equation for the water phase leads to the generalized form of the Darcy equation [26]:

$$\boldsymbol{v}^{ws} = \frac{\boldsymbol{k}}{\mu_w}[-\nabla p_w + \rho_w \mathbf{b}] \tag{6}$$

and the final form of the continuity equation for the water phase can be expressed as [26],

$$\left[\frac{(\alpha - n)}{K_s} + \frac{n}{K_w}\right]\frac{\partial p_w}{\partial t} + \alpha \nabla \cdot \mathbf{v_s} + \nabla \cdot [\mathbf{k}(-\nabla p_w + \rho_w(\mathbf{b}))] = 0 \tag{7}$$

where $\mathbf{k}$ is the permeability tensor and μ_w is the value of water viscosity. K_w and $\mathbf{v_s}$ are defined as the bulk modulus and the Darcy velocity for the water phase, respectively.

The boundary conditions include the imposed tractions and water fluxes on the outward boundaries and the relevant prescribed essential boundary conditions for solid displacements and water pressures,

$$\begin{aligned} &\boldsymbol{u} = \bar{\boldsymbol{u}} \quad \text{on } \Gamma_u \\ &\boldsymbol{p_w} = \bar{\boldsymbol{p}}_{\boldsymbol{w}} \quad \text{on } \Gamma_{p_w} \end{aligned} \tag{8}$$

$$\begin{aligned} &\boldsymbol{\sigma} \cdot \boldsymbol{n}_{\Gamma_c} = \bar{\boldsymbol{t}} \quad \text{on } \Gamma_t \\ &\boldsymbol{v_w} \cdot \boldsymbol{n}_{\Gamma_c} = \overline{\boldsymbol{q_w}} \quad \text{on } \Gamma_{q_w} \end{aligned} \tag{9}$$

Along with the external boundaries, extra conditions are satisfied at fracture surfaces to account for compatibility of transformed cohesive tractions with the cohesive zone model adopted for the governing mechanical behavior of the fracture and the role of fluid exchange through the crack faces. Assumption of a cohesive zone model leads to elimination of infinite stresses at the crack tips, which is more realistic for porous-like materials. In this model, the crack is assumed to be fully opened when the values of openings exceed the critical openings inferred from the governing interface law. The imposition of exchanging cohesive forces along the fracture surfaces is performed as an internal boundary condition. The cohesive zones are assumed to have a zero thickness across the crack face and the stresses are computed based on the traction-separation cohesive law. Water may flow freely through the fractured zone and the fracture walls act as permeable defects, which lead

to changes in the hydro-mechanical behavior of the defected zones. Flow of water through the fracture faces leads to discontinuous water pressure gradients (discontinuous water flows), whereas the water pressure is assumed to be constant and uniform across the crack width. For the mass transfer along the fracture, the continuity equation of the whole medium is linked with the balance of mass equation derived for a control volume of the fracture line [37]. In order to model the hydro-mechanical behavior of the fracture, the following additional internal boundary conditions are satisfied,

$$\begin{aligned} &\boldsymbol{\sigma}\cdot\boldsymbol{n}_{\Gamma_c} = \bar{\boldsymbol{t}}_{\boldsymbol{c}} = \bar{\boldsymbol{t}}_{\boldsymbol{d}} - \alpha p_w \boldsymbol{n}_{\Gamma_c} \quad \text{on } \Gamma_c \\ &[\![\boldsymbol{v}_{\boldsymbol{w}}]\!]\cdot\boldsymbol{n}_{\Gamma_c} = \bar{q}_{wd} \quad \text{on } \Gamma_c \end{aligned} \tag{10}$$

where n_{Γ_c} is the unit normal vector to the crack surface, $\boldsymbol{t_d}$ is the cohesive traction resulted from the cohesive law and p_w is the value of water pressure imposed on the crack surface.

Different rules for the governing mechanical behavior of the cohesive crack are used in this paper. The linear, bi-linear and exponential non-linear traction-separation laws are depicted in Fig. 2. It is noted that without the loss of generality, only the effect of normal tractions is considered and exceeding the normal stress at the nearest point to the fracture tip from the tensile threshold of the material is used as the criterion for crack propagation. When a crack is perceived to be propagated, a predefined small crack length increment along the normal to the maximum hoop stress direction is added to the current crack configuration. Eq. (11) defines the angle of crack growth direction in terms of the stress intensity factors at a crack tip [61],

$$\theta = 2\arctan\frac{1}{4}\left(\frac{K_I}{K_{II}} \pm \sqrt{\left(\frac{K_I}{K_{II}}\right)^2 + 8}\right) \tag{11}$$

where the stress intensity factors K_I and K_{II} are computed based on the domain form of the interaction integral [11].

Next, the water flux exchange terms (10), introduced to the total continuity equation of water (7) to account for transmit of water through the fracture walls, are elaborated. Considering an arbitrary volume of the fractured zone in a local coordinate system x'–y', in which the horizontal axis is placed along the fracture line, one can write the continuity equation for the water flow in an average sense:

$$\int_{-h}^{h}\left[\frac{1}{Q_{wd}}\dot{p_w} + \alpha\nabla\cdot\dot{u} + \nabla\cdot\boldsymbol{v}^{ws}\right]dy = 0 \tag{12}$$

where $2h$ represents the value of crack opening. The water pressure is assumed to be constant across the fracture width, and linear variations for horizontal solid phase velocities are considered. Simplifying the gradients of water pressure and solid displacement time derivatives and inserting the Darcy Eq. (6) for water phase velocities, the final form of the expression for the exchanging flux term $\bar{q}_{wd}$ in (10) is obtained [37],

$$\begin{aligned} \bar{q}_{wd} = &\frac{2h}{Q_{ww}}\frac{\partial p_w}{\partial t} + \alpha[\![w_s]\!] + 2h\alpha < \frac{\partial \mathbf{v_s}}{\partial x} \\ &> -\frac{\partial}{\partial x}\left(2\mathbf{k_{wd}}\frac{\partial p_w}{\partial x}\right) + \left(2\mathbf{k_{wd}}\frac{\partial p_w}{\partial x}\frac{\partial h}{\partial x}\right) \end{aligned} \tag{13}$$

where $\langle\bigstar\rangle$ and $[\![\bigstar]\!]$ represent the average and difference of variables at the two opposite sides of the crack, respectively. $\mathbf{k_{wd}}$ is the permeability tensor in the fractured region and $\bar{q}_{wd}$ represents the rate of water flux exchange between the damaged and undamaged surrounding media, obtained by the satisfaction of continuity equation for water flow through an arbitrary control volume in the fractured zone.

3. Numerical model

3.1. Weak formulation

In this section, the weak form of the governing equations is derived and discretization of the unknowns in the framework of the EFG meshfree method is developed using the MLS shape functions. As the MLS shape functions do not satisfy the Kronecker delta function property, which facilitates the imposition of essential boundaries, the Lagrange multipliers method is adopted to impose the essential boundary conditions. No gas pressure is present in the assumed saturated domain and the whole void space is filled with the liquid water. Solid displacements and water pressures are considered as the main unknowns, which is compatible with the governing equations of fully coupled porous media, discussed in the previous section.

Applying the weighted residual method to Eqs. (1) and (7), along with the corresponding boundary conditions of (9) and (10), the final constrained weak form of the governing equations are obtained,

$$\begin{aligned} &\int_\Omega \delta(\boldsymbol{L_u u})^T(\boldsymbol{\sigma})d\Omega - \int_\Omega \delta\boldsymbol{u}^T\boldsymbol{b}\,d\Omega - \int_{\Gamma_u}\delta\boldsymbol{u}^T\boldsymbol{t}\,d\Gamma_u \\ &+ \int_{\Gamma_c}\delta[\![\boldsymbol{u}]\!]^T\bar{\boldsymbol{t}}_{\boldsymbol{c}}\,d\Gamma_c - \delta\left(\int_{\Gamma_u}\lambda_u^T(u-\bar{u})d\Gamma_u\right) = 0 \end{aligned} \tag{14}$$

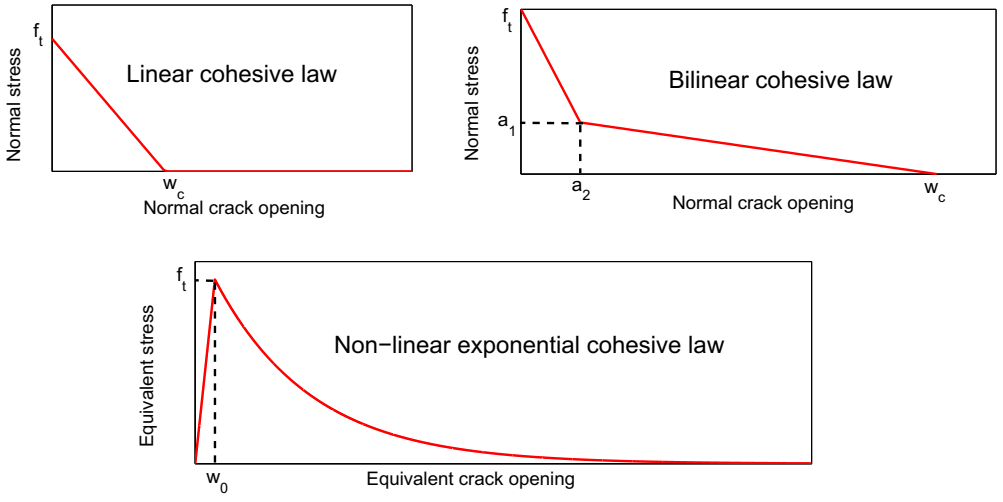

Fig. 2. Linear, bilinear and exponential cohesive laws.

$$\int_\Omega \delta(p_w)^T \cdot \left[\frac{(\alpha-n)}{K_s}+\frac{n}{K_w}\right]\frac{\partial p_w}{\partial t}\,d\Omega + \int_\Omega \delta(p_w)^T \cdot \alpha \mathbf{m}^{\mathbf{T}}\mathbf{L_u}\frac{\partial \mathbf{u}}{\partial t}\,d\Omega + \int_\Omega \delta(L_{p_w}p_w)^T \cdot [\mathbf{k}(-\nabla p_w + \rho_w(\mathbf{b}))]d\Omega + \int_{\Gamma_c} \delta(p_w)^T q_{wd}^- \,d\Gamma_c + \delta\left(\int_{\Gamma_{p_w}} \lambda_{p_w}^T (p_w - \bar{p_w})d\Gamma_{p_w}\right) = 0 \tag{15}$$

$\delta(\boldsymbol{u})$ and $\delta(p_w)$ represent the variations of solid displacement and water pressure, respectively and act as the weighting functions in the proposed Galerkin weak form of the fully coupled saturated porous medium. Note that the last parts are introduced due to the enforcement of essential boundary conditions for solid displacements and water pressure in the context of the Lagrange multipliers method. The integrals on the crack surfaces (Γ_c) are the interfacial terms resulted from the hydro-mechanical exchange of tractions and fluxes through the fracture walls. The differential operators $\mathbf{L_u}$ and $\mathbf{L_p}$ are defined as,

$$\mathbf{L_u} = \begin{bmatrix} \frac{\partial}{\partial x} & 0 \\ 0 & \frac{\partial}{\partial y} \\ \frac{\partial}{\partial y} & \frac{\partial}{\partial x} \end{bmatrix}, \qquad \mathbf{L_p} = \begin{bmatrix} \frac{\partial}{\partial x} \\ \frac{\partial}{\partial y} \end{bmatrix} \tag{16}$$

3.2. Numerical discretization and non-linear solution procedure

To capture discontinuities in solid and water pressure phases, enrichment of the local variables are written in the following format at an arbitrary point x of the domain,

$$u^h(x) = \sum_{I=1}^{n} \Phi_I^{u,std}(x)u_I^{std} + \sum_{I=1}^{n} \Phi_I^{u,std}(x)H(x)u_I^{enr},$$
$$p_w^h(x) = \sum_{I=1}^{n} \Phi_I^{p_w,std}(x)\left(p_w^{std}\right)_I + \sum_{I=1}^{n} \Phi_I^{p_w,std}(x)\Upsilon_{p_w}(x)\left(p_w^{enr}\right)_I, \tag{17}$$

where $\Phi_I^{u,std}$ and $\Phi_I^{p_w,std}$ stand for the MLS shape functions for discretization of the solid displacements and water pressures, respectively. $H(x)$ is the Heaviside enrichment function (18) representing the discontinuous part of the displacement field. To account for continuous water pressure but with discontinuous normal gradients, $\Upsilon_{p_w}(x)$ is selected as the modified distance enrichment function (19), which also eliminates the loss of precision in the blending domain [21],

$$H(x) = \begin{cases} 1 & \text{if } (x-x^{cr})\cdot n \geqslant 0 \\ 0 & \text{otherwise} \end{cases} \tag{18}$$

$$\Upsilon_{p_w}(x) = \sum\nolimits_I \Phi_I^{p_w}(x)|\zeta_I| - \left|\sum_I \Phi_I^{p_w}(x)\zeta_I\right|. \tag{19}$$

Insertion of the enriched approximation (17) into the weak form equations of (14) and (15) results in the complete discretized set of constrained equations for the fully coupled saturated deforming porous medium,

$$\int_\Omega \mathbf{B}^{\mathbf{T},\mathbf{n+1}}\boldsymbol{\sigma}''d\Omega - \mathbf{C_{sw}^{n+1}}\mathbf{P_w^{n+1}} + \mathbf{f_{coh}^{n+1}} = \mathbf{F_u^{n+1}} - \left[\mathbf{G_{\bar{u}}^T}\boldsymbol{\lambda}_{\boldsymbol{u}}^{\boldsymbol{n+1}}\right]$$
$$\mathbf{C_{ws}^{n+1}}\dot{\mathbf{U}}^{\mathbf{n+1}} + \mathbf{P_{ww}^{n+1}}\dot{\mathbf{P}}_{\mathbf{w}}^{\mathbf{n+1}} + \mathbf{H_{ww}^{n+1}}\mathbf{P_w^{n+1}} + \mathbf{Q_{mass}^{n+1}} = \mathbf{F_w^{n+1}} - \left[\boldsymbol{G}_{\bar{p}_w}^{\boldsymbol{T}}\boldsymbol{\lambda}_{\boldsymbol{p_w}}^{\boldsymbol{n+1}}\right] \tag{20}$$

which is naturally coupled with the following constraint equations for imposition of essential boundaries:

$$\overline{\boldsymbol{U}} = \boldsymbol{G}_{\bar{\boldsymbol{u}}}\boldsymbol{U}^{\boldsymbol{n+1}}$$
$$\bar{\boldsymbol{P}}_{\boldsymbol{w}} = \boldsymbol{G}_{\bar{p}_{\boldsymbol{w}}}\boldsymbol{P}_{\boldsymbol{w}}^{\boldsymbol{n+1}} \tag{21}$$

along with the following internal force and flux vectors,

$$\mathbf{f_{coh}} = \int_{\Gamma_c} [\![\mathbf{N_u^T}]\!]\bar{\mathbf{t}}_{\mathbf{c}}\,d\Gamma_c$$
$$\mathbf{Q_{mass}} = \int_{\Gamma_c} \mathbf{N_{p_w}^T} q_{wd}^-\,d\Gamma_c \tag{22}$$

where

$$\mathbf{K} = \int_\Omega \mathbf{B_u^T}\mathbf{D}\mathbf{B_u}\,d\Omega$$
$$\mathbf{C_{sw}} = \int_\Omega \mathbf{B_u^T}\alpha\mathbf{m}\mathbf{N_{p_w}}\,d\Omega$$
$$\mathbf{C_{ws}} = \int_\Omega \mathbf{N_{p_w}^T}\alpha\mathbf{m}^{\mathbf{T}}.\mathbf{B_u}\,d\Omega$$
$$\mathbf{P_{ww}} = \int_\Omega \mathbf{N_{p_w}^T}.\left(\frac{1}{Q_{ww}}\right)\cdot\mathbf{N_{p_w}}\,d\Omega$$
$$\mathbf{H_{ww}} = \int_\Omega (\mathbf{L_{p_w}}\mathbf{N_{p_w}})^T\mathbf{k}(\mathbf{L_{p_w}}\mathbf{N_{p_w}})d\Omega \tag{23}$$
$$(\mathbf{G_{\bar{u}}})_{IK} = -\int_{\Gamma_u} \Phi_I^u N_k\,d\Gamma_u$$
$$(\mathbf{G_{\bar{p}_w}})_{IK} = -\int_{\Gamma_{p_w}} \Phi_I^{p_w} N_k\,d\Gamma_{p_w}$$
$$N_k(x) = \delta(x - x_k)$$

x_k is defined as the set of nodes placed along the essential boundaries and $\mathbf{m} = [1\ 1\ 0]^T$, and

$$\mathbf{B_u} = \left[\mathbf{B_u^{std}} \quad \mathbf{B_u^H}\right]$$
$$\mathbf{N_u} = \left[\mathbf{N_u^{std}} \quad \mathbf{N_u^H}\right] \tag{24}$$
$$\mathbf{N_{pw}} = \left[\mathbf{N_{pw}^{std}} \quad \mathbf{N_{pw}^{\Upsilon}}\right]$$

It is noted that the terms $\mathbf{f_{coh}}$ and $\mathbf{Q_{mass}}$ are line integrals along the crack faces, which are computed by the Gaussian quadrature rule. These terms introduce non-linearity to the system of equations which are solved through a suitable non-linear strategy. Assuming a linear variation for derivatives of unknown variables in time

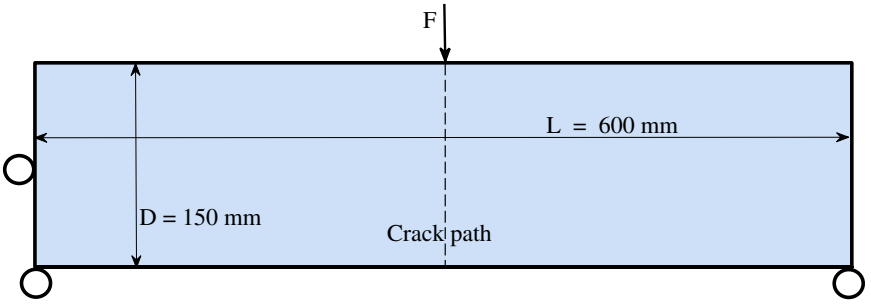

Fig. 3. Three-point bending beam.

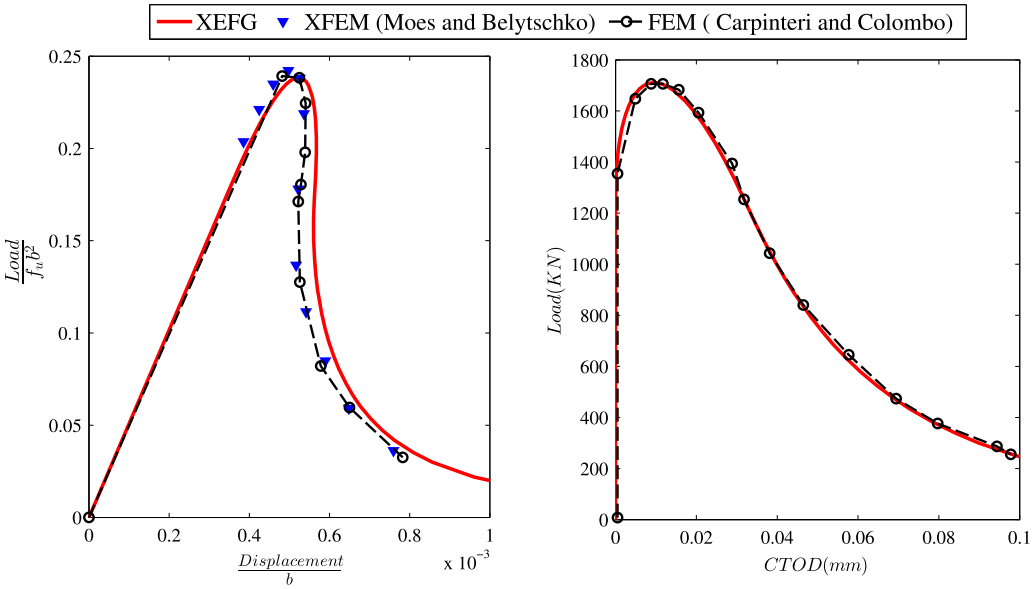

Fig. 4. Load–deflection and load–CTOD curves for $G_f = 0.05$ N/mm.

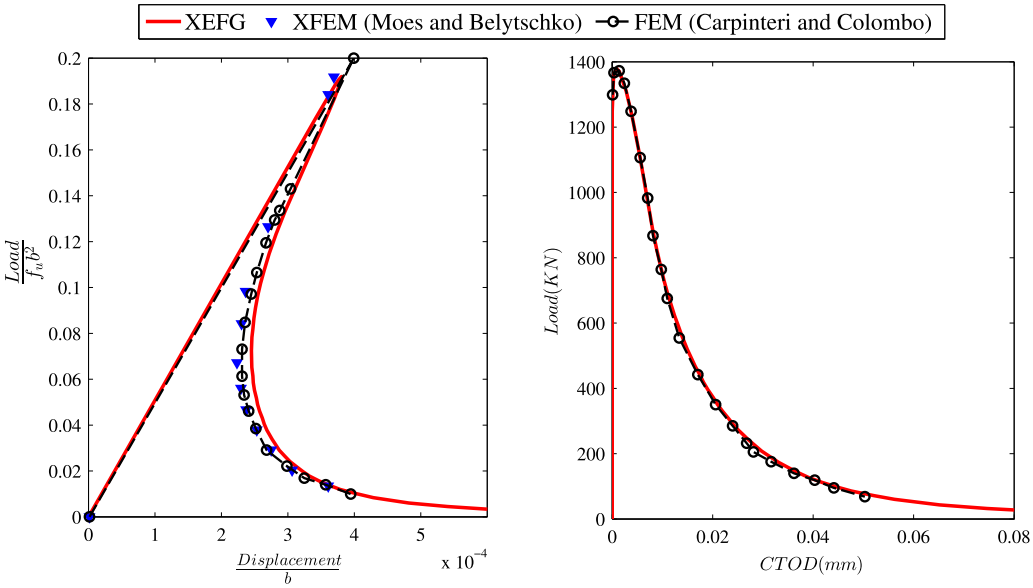

Fig. 5. Load–deflection and load–CTOD curves for $G_f = 0.01$ N/mm.

and using the Newton–Raphson algorithm, the final form of the discretized set of equations can be written as,

$$\begin{aligned}
\mathbf{R}_{\mathbf{u}}^{\mathbf{i},\mathbf{n}+1} &= \mathbf{K}\mathbf{U}^{\mathbf{i},\mathbf{n}+1} - \mathbf{C}_{\mathbf{sw}}\mathbf{P}_{\mathbf{w}}^{\mathbf{i},\mathbf{n}+1} + \mathbf{f}_{\mathbf{coh}}^{\mathbf{n}+1} - \mathbf{F}_{\mathbf{u}}^{\mathbf{n}+1} + \left[\mathbf{G}_{\bar{\mathbf{u}}}^{\mathbf{T}}\boldsymbol{\lambda}_{\mathbf{u}}^{\mathbf{n}+1}\right] \\
\mathbf{R}_{\mathbf{pw}}^{\mathbf{i},\mathbf{n}+1} &= \mathbf{C}_{\mathbf{ws}}^{\mathbf{n}+1}\left(\frac{\mathbf{U}^{\mathbf{n}+1}-\mathbf{U}^{\mathbf{n}}}{\Delta t}\right) + \mathbf{P}_{\mathbf{ww}}^{\mathbf{n}+1}\left(\frac{\mathbf{P}_{\mathbf{w}}^{\mathbf{n}+1}-\mathbf{P}_{\mathbf{w}}^{\mathbf{n}}}{\Delta t}\right) + \mathbf{H}_{\mathbf{ww}}^{\mathbf{n}+1}\mathbf{P}_{\mathbf{w}}^{\mathbf{n}+1} \\
&\quad + \mathbf{Q}_{\mathbf{mass}}^{\mathbf{n}+1} - \mathbf{F}_{\mathbf{w}}^{\mathbf{n}+1} + \left[\mathbf{G}_{\bar{\mathbf{p}}_{\mathbf{w}}}^{\mathbf{T}}\boldsymbol{\lambda}_{p_w}^{n+1}\right] \\
\boldsymbol{R}_{\lambda_u}^{i,n+1} &= \bar{\mathbf{U}} - \mathbf{G}_{\bar{\mathbf{u}}}\mathbf{U}^{\mathbf{n}+1}, \quad \boldsymbol{R}_{\lambda_{p_w}}^{i,n+1} = \bar{P_w} - \boldsymbol{G}_{\bar{p}_w}\boldsymbol{P}_{\boldsymbol{w}}^{\boldsymbol{n}+1}
\end{aligned} \tag{25}$$

and the unknown and residual vectors can be expressed by:

$$\mathbf{X}^{\mathbf{i},\mathbf{n}+1} = \begin{Bmatrix} \mathbf{U}^{\mathbf{i},\mathbf{n}+1} \\ \mathbf{P}_{\mathbf{w}}^{\mathbf{i},\mathbf{n}+1} \\ \boldsymbol{\lambda}_{\boldsymbol{u}}^{\boldsymbol{i},\boldsymbol{n}+1} \\ \boldsymbol{\lambda}_{\boldsymbol{p}_w}^{\boldsymbol{i},\boldsymbol{n}+1} \end{Bmatrix} \quad \mathbf{R}^{\mathbf{i},\mathbf{n}+1} = \begin{Bmatrix} \mathbf{R}_{\mathbf{u}}^{\mathbf{i},\mathbf{n}+1} \\ \mathbf{R}_{\mathbf{pw}}^{\mathbf{i},\mathbf{n}+1} \\ \boldsymbol{R}_{\lambda_u}^{i,n+1} \\ \boldsymbol{R}_{\lambda_{p_w}}^{i,n+1} \end{Bmatrix} \tag{26}$$

Differentiating the residual with respect to the unknowns vector **X**, gives the Jacobian matrix for the constrained system of equations,

$$\mathbf{J} = \begin{bmatrix} \mathbf{K} + \frac{\partial \mathbf{f}_{\mathbf{coh}}}{\partial \mathbf{u}} & -\mathbf{C}_{\mathbf{sw}} + \frac{\partial \mathbf{f}_{\mathbf{coh}}}{\partial p_w} & \mathbf{G}_{\bar{\mathbf{u}}}^{\mathbf{T}} & 0 \\ \frac{\mathbf{C}_{\mathbf{ws}}}{\Delta t} + \frac{\partial \mathbf{Q}_{\mathbf{mass}}}{\partial \mathbf{u}} & \frac{\mathbf{P}_{\mathbf{ww}}}{\Delta t} + \mathbf{H}_{\mathbf{ww}} + \frac{\partial \mathbf{Q}_{\mathbf{mass}}}{\partial p_w} & 0 & \mathbf{G}_{\bar{\mathbf{p}}_{\mathbf{w}}}^{\mathbf{T}} \\ -\mathbf{G}_{\bar{\mathbf{u}}} & 0 & 0 & 0 \\ 0 & -\mathbf{G}_{\bar{\mathbf{p}}_{\mathbf{w}}} & 0 & 0 \end{bmatrix} \tag{27}$$

The following fully coupled nonlinear system of equations should then be solved at each time step to compute the vector of unknown increments,

$$\mathbf{R}^{\mathbf{i}+\mathbf{1},\mathbf{n}+\mathbf{1}} = \mathbf{R}^{\mathbf{i},\mathbf{n}+1} + \mathbf{J}[\mathbf{dX}^{\mathbf{i}+\mathbf{1},\mathbf{n}+\mathbf{1}}] = 0 \tag{28}$$

$$[\mathbf{dX}^{\mathbf{i}+\mathbf{1},\mathbf{n}+\mathbf{1}}] = \begin{bmatrix} d\boldsymbol{U}^{\boldsymbol{i}+\mathbf{1},\boldsymbol{n}+\mathbf{1}} \\ d\boldsymbol{P}_{\boldsymbol{w}}^{\boldsymbol{i}+\mathbf{1},\boldsymbol{n}+\mathbf{1}} \\ d\boldsymbol{\lambda}_{\boldsymbol{u}}^{\boldsymbol{i},\boldsymbol{n}+1} \\ d\boldsymbol{\lambda}_{\boldsymbol{P}_w}^{\boldsymbol{i},\boldsymbol{n}+1} \end{bmatrix} = -\mathbf{J}^{-1}\mathbf{R}^{\mathbf{i},\mathbf{n}+1}. \tag{29}$$

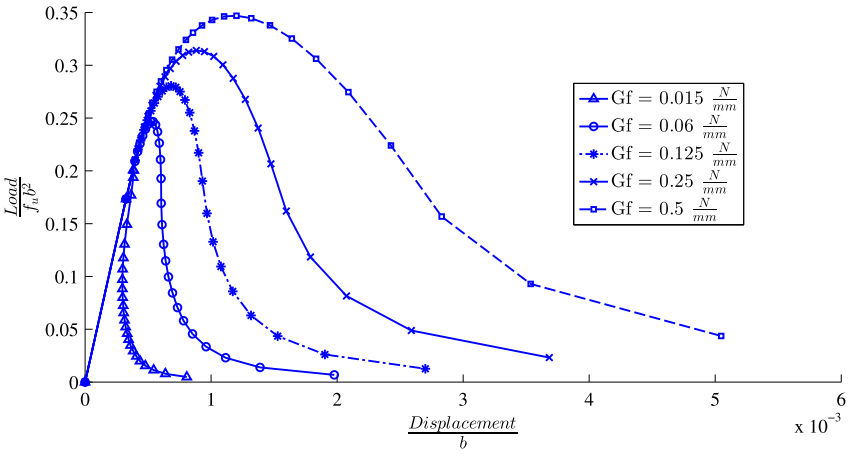

Fig. 6. Load–displacement curves for different values of G_f.

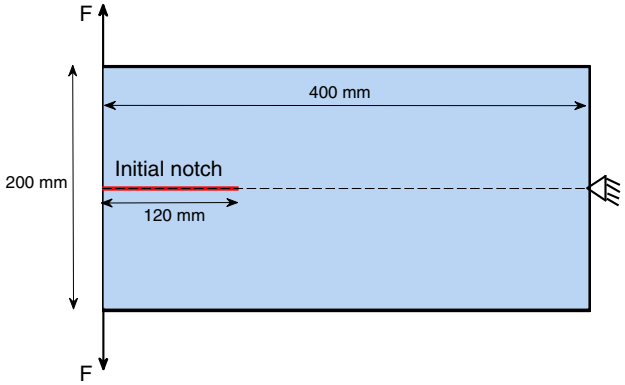

Fig. 7. Geometry of the double cantilever problem.

in which $\mathbf{R}^{i,n+1}$ is given in (25) and is computed as:

$$\mathbf{R}^{i,n+1} = \mathbf{J}\begin{bmatrix} \boldsymbol{U}^{i,n+1} \\ \boldsymbol{P}_w^{i,n+1} \\ \boldsymbol{\lambda}_u^{i,n+1} \\ \boldsymbol{\lambda}_{p_w}^{i,n+1} \end{bmatrix} - \begin{bmatrix} \boldsymbol{F}_u \\ \boldsymbol{F}_w \\ \overline{\boldsymbol{U}} \\ \overline{\boldsymbol{P}}_w \end{bmatrix} - \mathbf{P}^{n} \tag{30}$$

where $\mathbf{P}^{n}$ is the value of converged solution from the last time step of analysis:

$$\mathbf{P}^{n} = \begin{bmatrix} 0 \\ \boldsymbol{C}_{ws}\left(\frac{\boldsymbol{U}^{n}}{\Delta t}\right) + \boldsymbol{P}_{ww}\left(\frac{\boldsymbol{P}_w^{n}}{\Delta t}\right) \\ 0 \\ 0 \\ 0 \end{bmatrix} \tag{31}$$

Then, the unknowns vector is updated at each iteration until the required convergence criterion is satisfied:

$$\begin{bmatrix} \mathbf{U}^{i+1,n+1} \\ \mathbf{P}_w^{i+1,n+1} \\ \boldsymbol{\lambda}_u^{i+1,n+1} \\ \boldsymbol{\lambda}_{p_w}^{i+1,n+1} \end{bmatrix} = \begin{bmatrix} \mathbf{U}^{i,n+1} \\ \mathbf{P}_w^{i,n+1} \\ \boldsymbol{\lambda}_u^{i,n+1} \\ \boldsymbol{\lambda}_{p_w}^{i,n+1} \end{bmatrix} + \begin{bmatrix} d\mathbf{U}^{i+1,n+1} \\ d\mathbf{P}_w^{i+1,n+1} \\ d\boldsymbol{\lambda}_u^{i+1,n+1} \\ d\boldsymbol{\lambda}_{p_w}^{i+1,n+1} \end{bmatrix} \tag{32}$$

4. Numerical simulations

4.1. Cohesive crack propagation in a dry domain

In the first set of numerical solutions, it is assumed that no fluid phase is present in the analysis. The developed computer implementation is then verified by problems of cohesive crack propagation under pure mode I and mixed mode conditions. In the numerical simulations of this paper, an appropriate estimate for

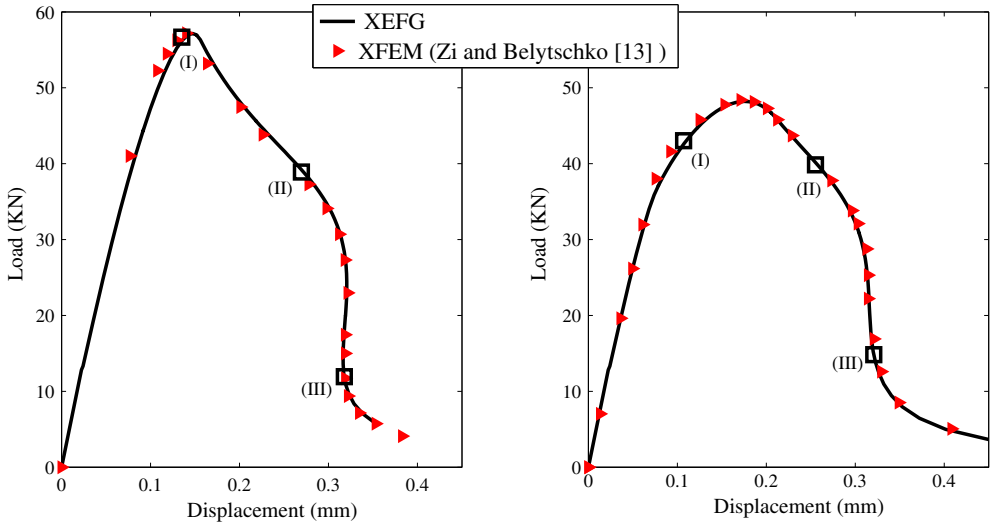

Fig. 8. Load–displacement curves for the double cantilever problem with linear cohesive law (left) and bilinear cohesive law (right).

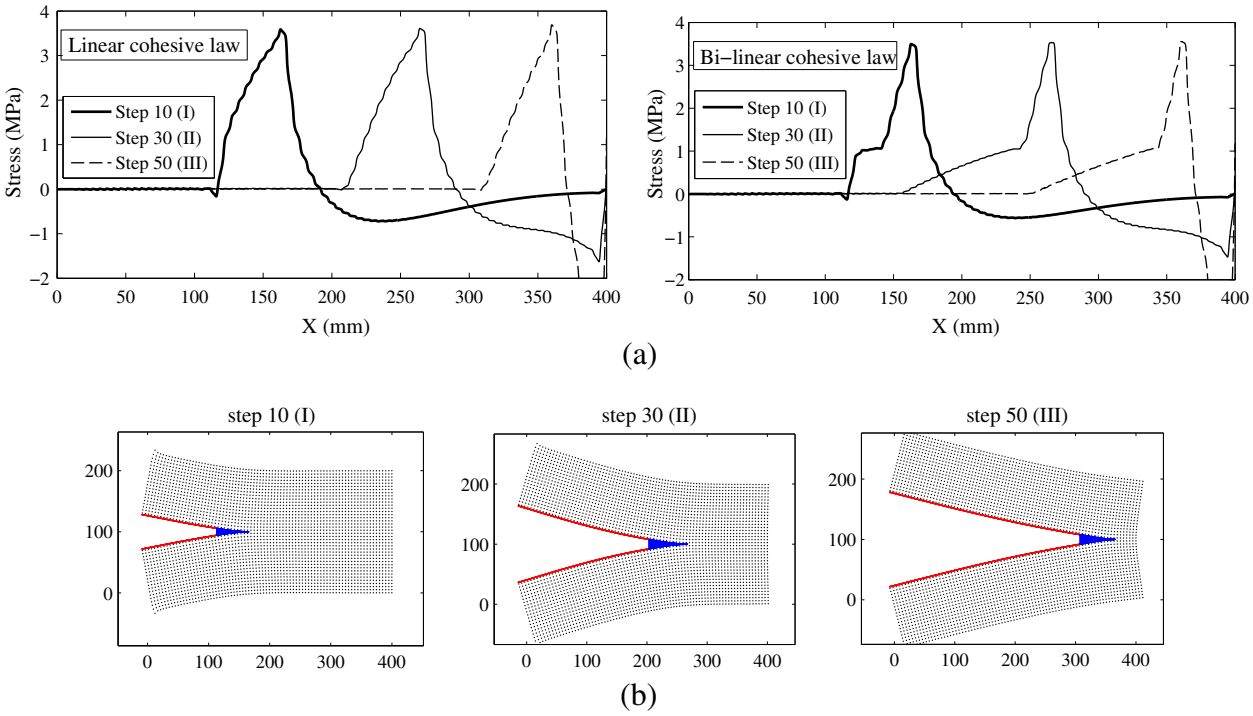

Fig. 9. (a) Vertical stress along the centerline of the beam, (b) deformed mesh and cohesive regions for different stages of crack propagation (linear cohesive law). Crack steps (I, II, III) are depicted in Fig. 8.

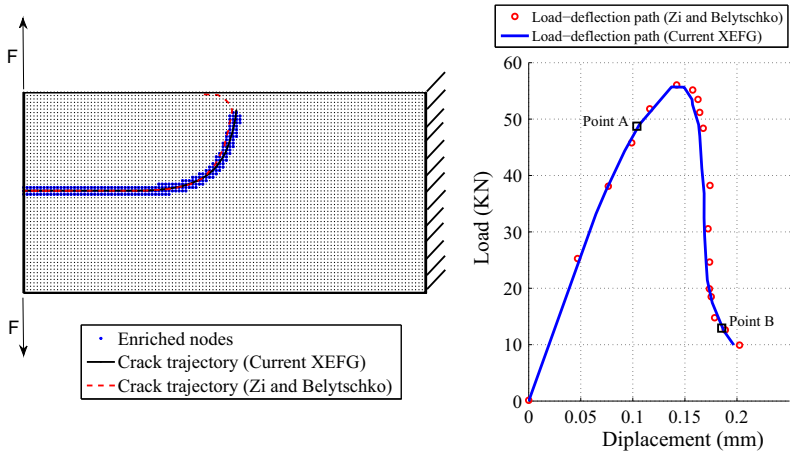

Fig. 10. Crack path and load–displacement curve for the mixed mode state of the double cantilever beam.

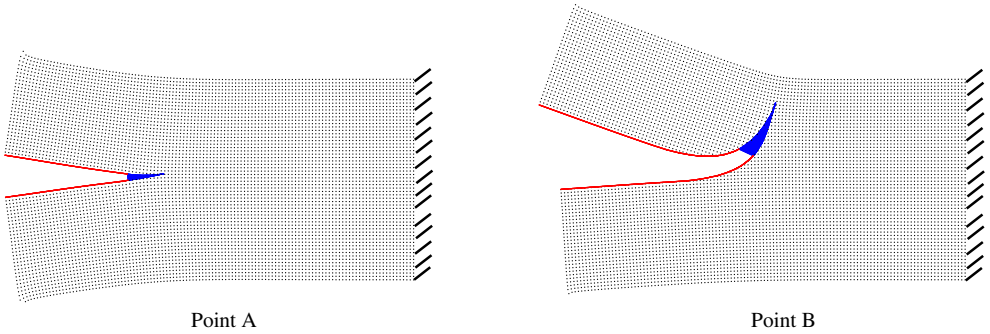

Fig. 11. Deformed mesh and the mixed mode crack paths, and the extents of cohesive zones are shown with the filled parts. Crack steps (A, B) are depicted in Fig. 10.

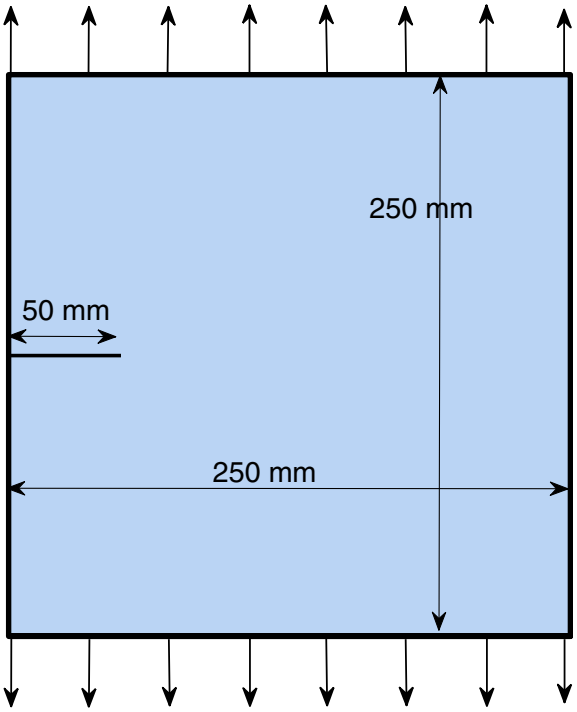

Fig. 12. Propagation of a cohesive crack in a saturated porous medium.

Table 1
Material properties for the cohesive crack problem.

Young's modulus (Pa)	25.85×10^9
Solid bulk modulus (Pa)	13.46×10^9
Fluid bulk modulus (Pa)	0.2×10^9
Water viscosity (MPa s)	1.0×10^{-9}
Intrinsic permeability of water (m^2)	2.78×10^{-9}
Poisson's ratio	0.18
Biot's coefficient	1
Tensile strength (MPa)	2.7
Fracture energy (N/mm)	0.095
Porosity	0.2

the size of the support domain has been numerically determined from a sensitivity analysis on several examples to ensure both optimum run-times and generation of smooth gradient distributions. This value is found to be 1.4 times of the average size of nodal spacings. Also, for all the numerical experiments, a linear basis function $(\mathbf{p}^{\mathbf{T}}(\mathbf{x}) = \{1\ x\ y\})$ is adopted.

4.1.1. Three-point-bending specimen

This problem has been solved extensively by various authors [6,61,62] using the conventional FEM and the extended finite element analysis (XFEM). A simply supported beam of dimensions $600 \times 150 \times 50$ mm is considered. Horizontal displacements are eliminated by fixing the left edge along the x direction, as shown in Fig. 3. The problem is solved with the Poisson's ratio of 0.1 and the Young's modulus of 36500 MPa in the plane strain condition. The linear cohesive law with $f_t = 3.19$ MPa is adopted and a uniform nodal arrangement of 80×30 is used. It is assumed that the fracture is nucleated at the center line when the maximum tensile strength (f_t) is reached. Different values of G_f are adopted. As the beam is loaded in the pure mode I condition, the crack path is predefined along a vertical path, as shown in Fig. 3.

Variations of load–deflection and the load versus crack tip opening displacements (CTOD) are shown in Fig. 4 for the fracture energy of 0.05 N/mm. Both results are in good agreement with the reference solutions of Carpinteri and Colombo [6] and Moes and Belytschko (XFEM) [61]. The fracture energy for this case is high enough to prevent a sharp snap-back instability.

The fracture energy is now further reduced to a value of 0.01 N/mm, which results in a small value for the critical opening displacement $\left(w_c = \frac{2 \times G_f}{f_t}\right)$. As a result, a smaller value for the cohesive zone length is obtained, which means that larger parts of crack surfaces are fully opened with zero cohesive tractions. As shown in Fig. 5, good agreements between the present and reference results are obtained. It should be noted that due to existence of snap-back in the load–displacement curves, standard displacement or load control analyses fail and appropriate crack length increment strategies need to be exploited. Fig. 6 shows the results from different values of fracture energy, which ranges from a very large value of 0.5 N/mm for which no snap-back is present, and descends to a low value of 0.015 N/mm, which results in a sharp snap-back.

4.1.2. Double cantilever beam

To further verify the cohesive formulation, the double cantilever beam with a cohesive crack is examined. The problem has previously been solved by Zi and Belytschko [13] using XFEM with no crack tip enrichments and especial crack tip elements that allowed for arbitrary placement of the crack tip.

A 400×200 mm beam is considered with the boundary conditions shown in Fig. 7 and the uniform nodal arrangement of 80×40 is used. A traction-free pre-notch of 120 mm length is placed at the center line of the beam, and a pure mode I condition prevails. Material properties for the bulk are $E = 36500$ MPa and $\nu = 0.18$. The problem is solved under the plane strain condition.

Two different linear and bilinear cohesive laws are examined for this problem. The tensile strength (f_t) is taken as 3.19 MPa and the fracture energy is equal to 0.095 N/mm for the linear cohesive law, while for the bi-linear cohesive law: $a_1 = 1$ MPa, $a_2 = 0.008$ mm and $w_c = 0.07$ mm (see Fig. 2).

The predicted load–displacement curves for the two cohesive laws are depicted in Fig. 8, which show a good agreement with the reference results reported by Zi and Belytschko [13]. Fig. 9 shows variations of vertical stress σ_{yy} along the crack line, obtained by the linear and bi-linear cohesive laws at three different steps of crack propagation. This figure further compares the effect of different cohesive laws on the stress state along the fracture line. In addition, the deformed configurations illustrate the extent of cohesive zones (filled area) at three different steps of the crack propagation.

Finally, the mixed mode cohesive crack propagation is analyzed by moving upward the notch 2 mm from the centerline of the beam. As a result, the crack path is expected to curve towards the upper edge of the plate. Also in order to prevent the beam from rotations, the right edge is fully clamped. In this case, the nodal arrangement of 120×60 is used. The resulted crack path and load–deflection curve are shown in Fig. 10, which verifies the capability of the developed XEFG algorithm in reproducing the results of a mixed mode cohesive crack propagation. Fig. 11, shows the deformed mesh and the extent of cohesive process zones at different stages of the mixed mode crack propagation for the linear cohesive law.

4.2. Cohesive crack propagation with coupling active water pressure

In this section, the full effect of coupling between solid and liquid phases is considered. Two distinct cases are studied in the numerical analysis: one without the mass exchange along the crack walls and the other with introducing the coupling term (13).

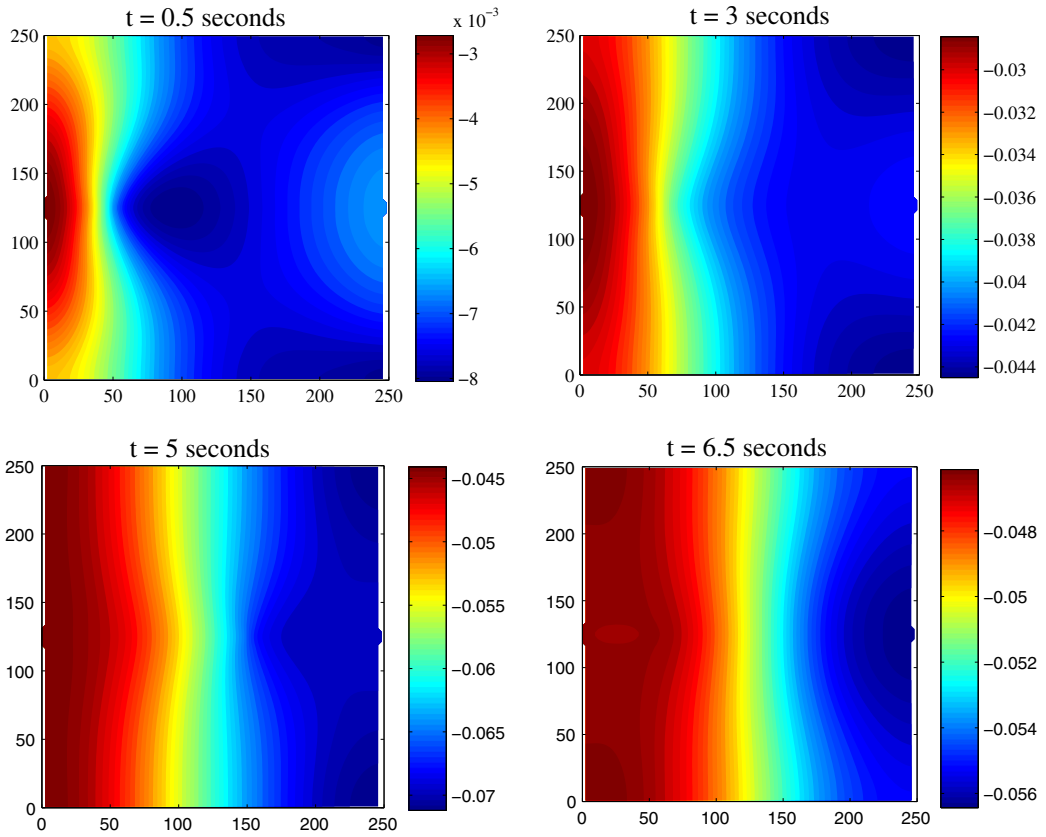

Fig. 13. Water pressures at different times of the analysis for the mode I cohesive crack propagation in the saturated porous material with no coupling term (values in MPa).

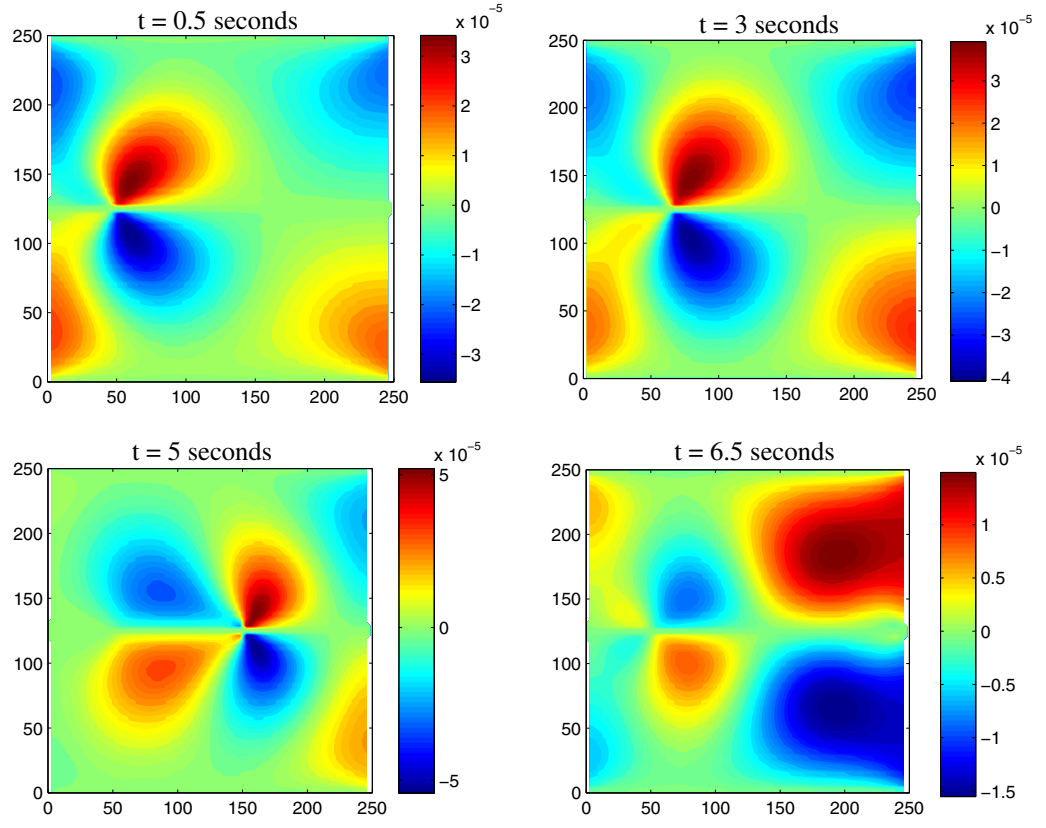

Fig. 14. Vertical gradients of the water pressure for the mode I problem with no coupling term (values in MPa/mm).

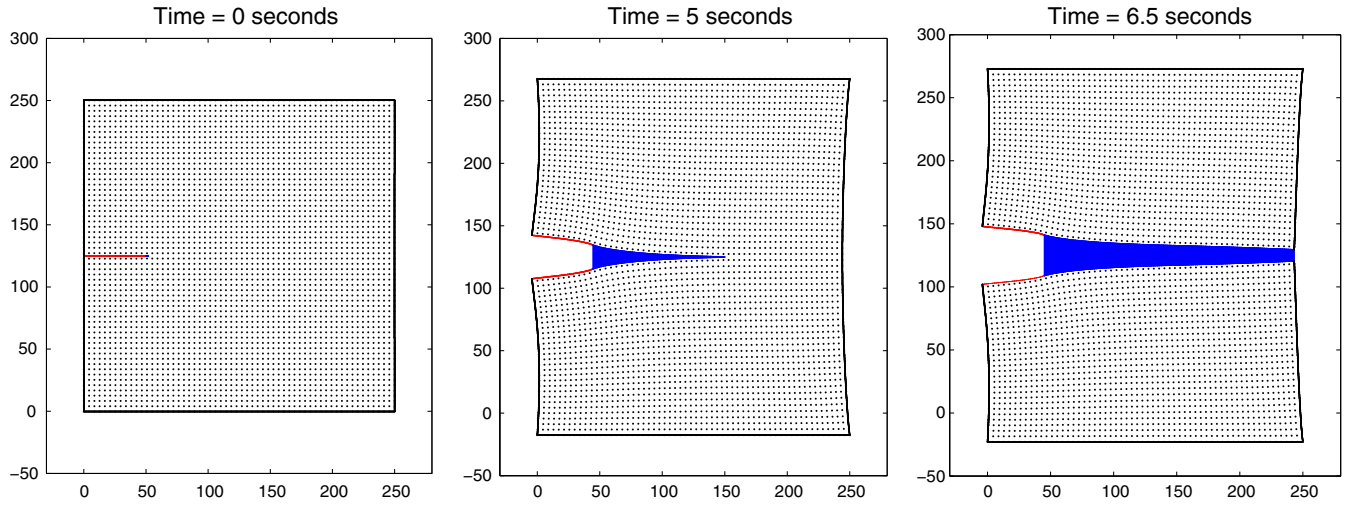

Fig. 15. Deformed mesh and the cohesive zone for the saturated cohesive crack test at different propagation stages (magnified by 1500×).

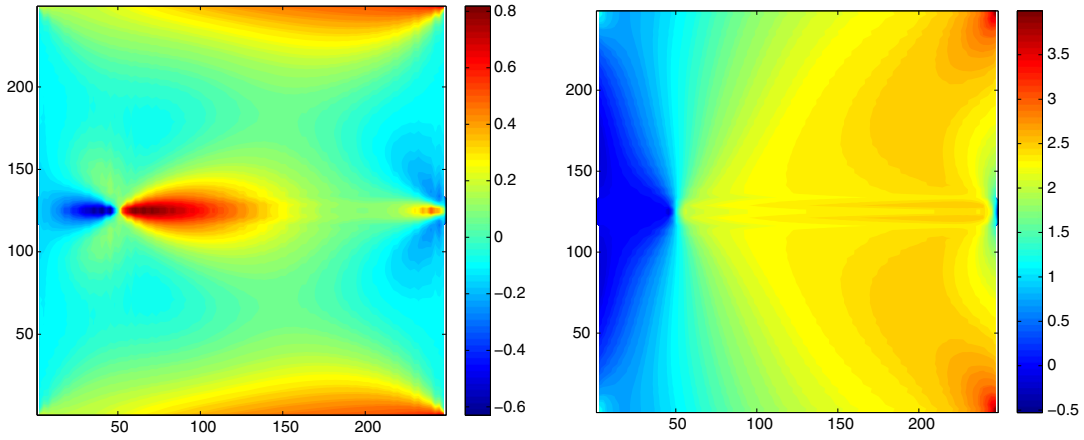

Fig. 16. Variations of σ_{xx} (left) and σ_{yy} (right) at the final step (values in MPa).

4.2.1. Mode I cohesive crack test

In this example, the cohesive crack test in a porous medium is considered. This problem was previously solved in [37–39] using the extended finite element method. An square plate with dimensions 250 × 250 mm and an initial notch of 50 mm length along the centerline is considered. Upper and lower edges of the domain are stretched with a fixed vertical velocity $\dot{u}_y = 2.35 \times 10^{-3}$ mm/s, while the horizontal displacements are fully constrained. Geometry and the boundary conditions are depicted in Fig. 12. The problem is solved for two different states: full coupling of fluid phase and with no fluid coupling involved. In the former case, the effect of mass coupling fluxes are considered along the whole fracture length.

Material properties for this problem are summarized in Table 1. Fixed displacements are exerted as a prescribed linear displacement in time. Normal stresses at the crack tip are checked in each time step of analysis and a new crack segment is introduced if this value exceeds the tensile threshold of the material (f_t). The problem is solved with the time step value of 0.05 s, and analysis is continued until the cohesive fracture propagates and reaches to the right edge. A plane strain condition is assumed and a uniform set of 60 × 60 nodal arrangement is used.

For the case I, where no mass exchange along the fracture walls is assumed, Fig. 13 shows the value of water pressures at four different time steps of the analysis, while Fig. 14 shows the corresponding values for the vertical gradients of water pressure. It is clearly observed that in the absence of any coupling term, distribution of the water pressure in the fractured medium is the same as an intact medium; the water flows through the fracture as it does in the bulk material.

The deformed mesh and the developed cohesive zone regions are depicted in Fig. 15. Fig. 16 shows the value of vertical and horizontal stress distributions in the final time step of the analysis, clearly showing that even when the crack is fully developed in the domain, crack walls remain closed and still transfer the vertical stresses.

Next, the effect of interfacial coupling terms are assessed. Values of water pressure and the corresponding vertical gradients are depicted in Figs. 17 and 18. It is clear that as the flux terms are integrated and imposed on the crack interface integral points, highly concentrated values for the water pressure at the fracture line with discontinuous vertical gradients are generated. Introduction of the modified distance function (19) results in a discontinuity in water velocity field (first gradients of the water pressures normal to the fracture) along the fracture sides, as shown in Fig. 18. Also, it is noted that in contrast to [37], both the initial notch and the developed cohesive parts are assumed to be involved with the mass exchange.

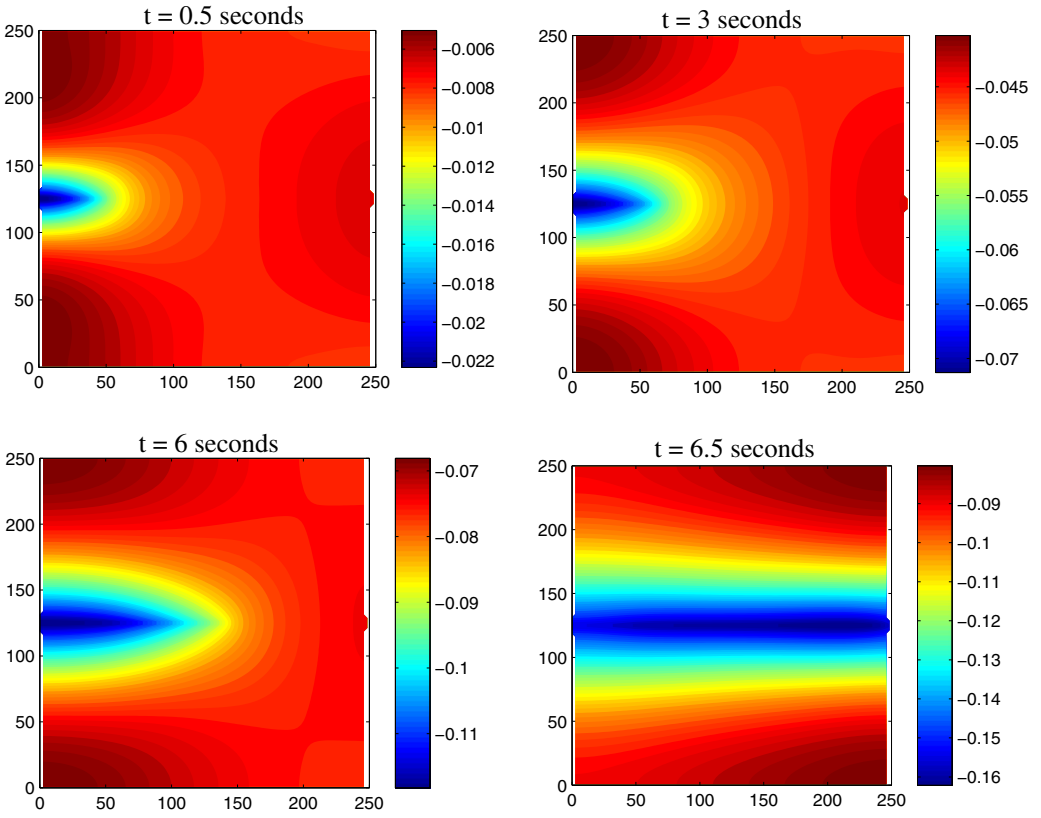

Fig. 17. Water pressure for the mode I case with mass exchange across the fracture walls (values in MPa).

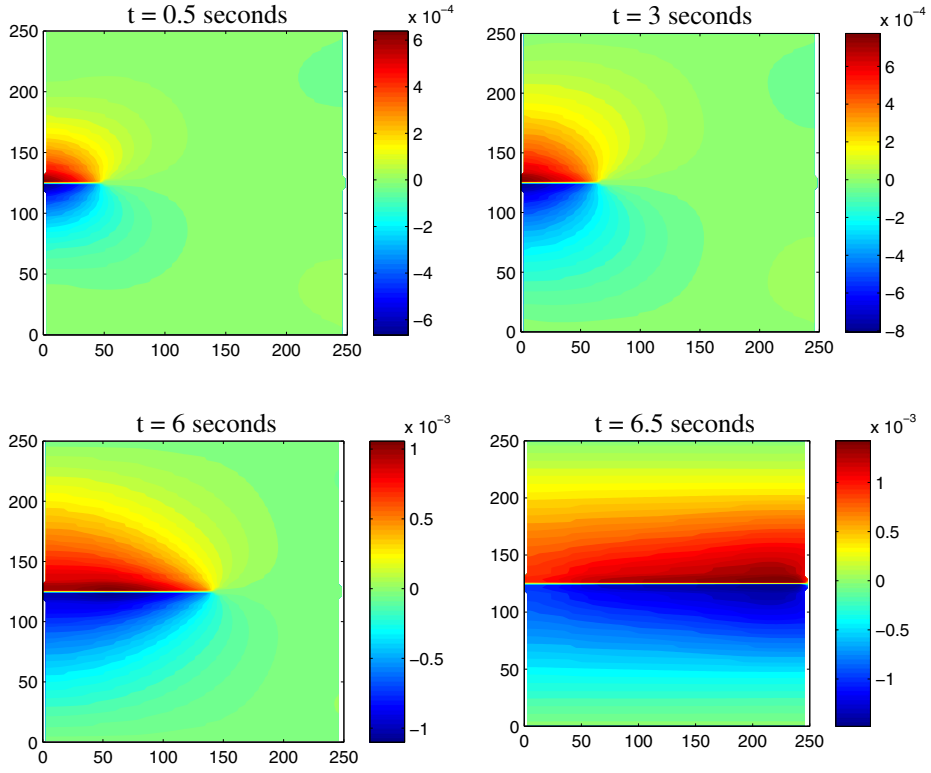

Fig. 18. Vertical water pressure gradients for the Mode I case with mass exchange across the fracture walls (values in MPa/mm).

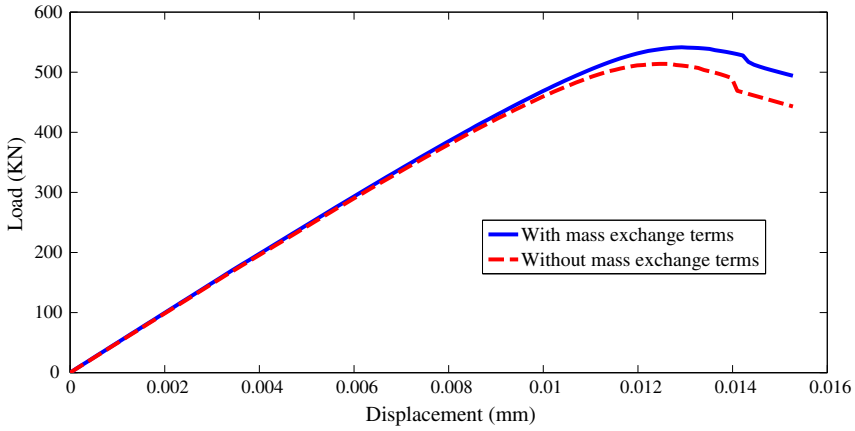

Fig. 19. Load–displacement curves.

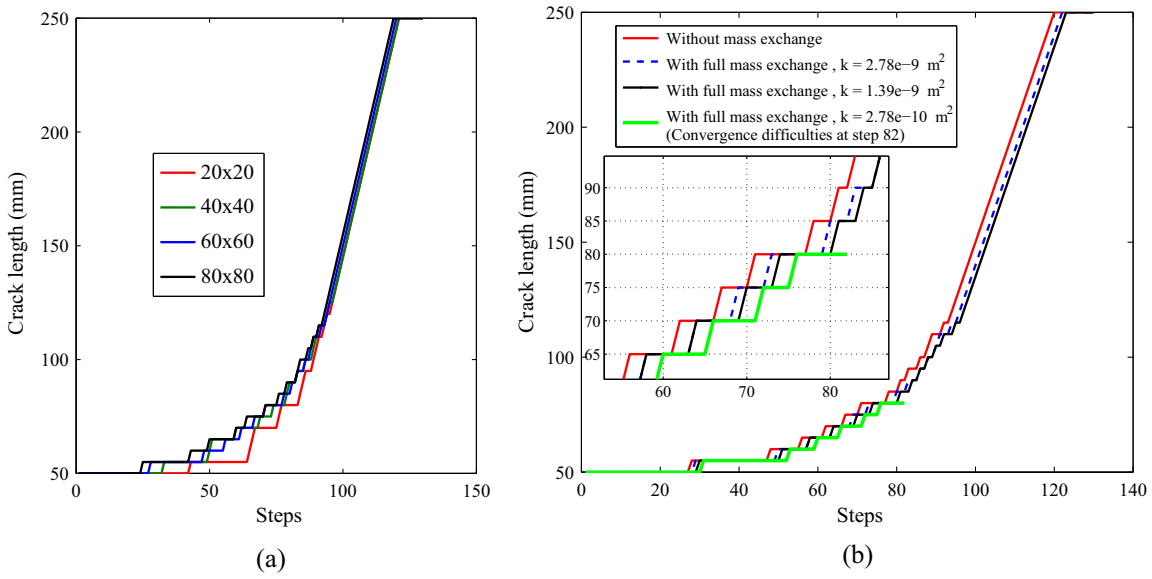

Fig. 20. (a) Comparison of crack length histories for different nodal densities. (b) The effect of coupling on crack path histories – convergence difficulties are encountered for $k \leqslant 2.78 \times 10^{-10}$ m².

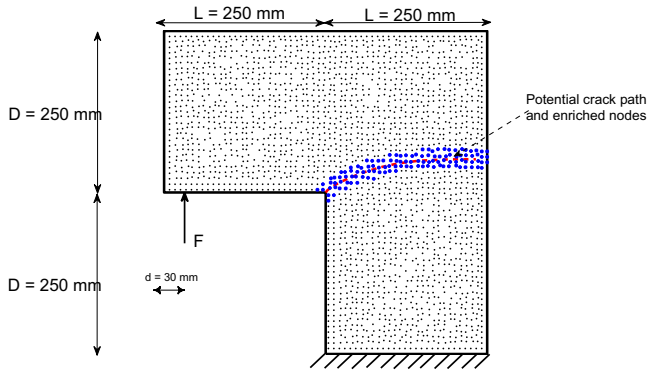

Fig. 21. L-shaped panel geometry and enriched nodes – unstructured mesh.

The high value of water pressure along the fracture surfaces leads to an increase in the load bearing capacity of the fracturing porous domain. In fact, the fracture walls are compressed due to significant water pressures for the mass exchange case. This effect can be observed in the load–deflection curves of Fig. 19, where the two cases with no coupling and with full coupling terms are compared.

Table 2
Material properties for the L-shaped panel.

Young's modulus (MPa)	20×10^3
Solid bulk modulus (Pa)	13.46×10^9
Fluid bulk modulus (Pa)	0.2×10^9
Water viscosity (MPa s)	1.0×10^{-9}
Intrinsic permeability of water (m²)	2.78×10^{-7}
Poisson's ratio	0.18
Biot's coefficient	1
Tensile strength (MPa)	2.5
Fracture energy (N/mm)	0.13
Porosity	0.2

The crack length histories for the current propagation test using different nodal arrangements are depicted in Fig. 20a, which shows the insensitivity of the results. Also, the convergence of the crack path histories is observed in Fig. 20b, which suggests that in the case of full coupling, the crack is initiated, propagated and reached to the right edge of the domain slightly later than the case of no mass exchange coupling. This behavior was also reported in [39],

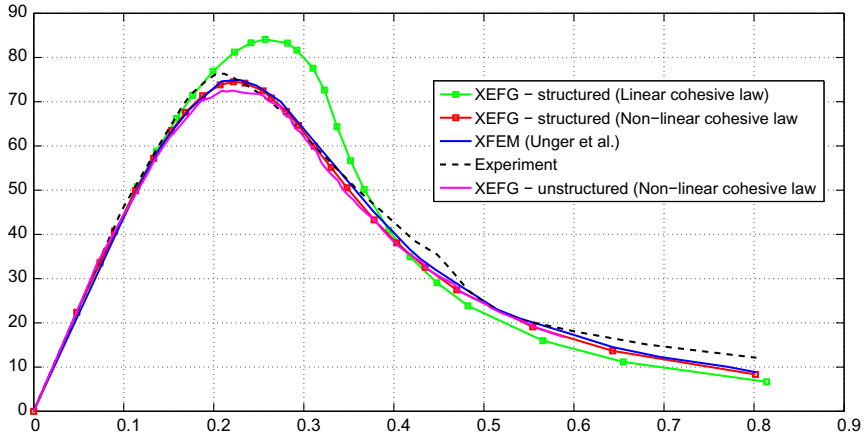

Fig. 22. Load–displacement curves for the mixed mode L-shaped panel.

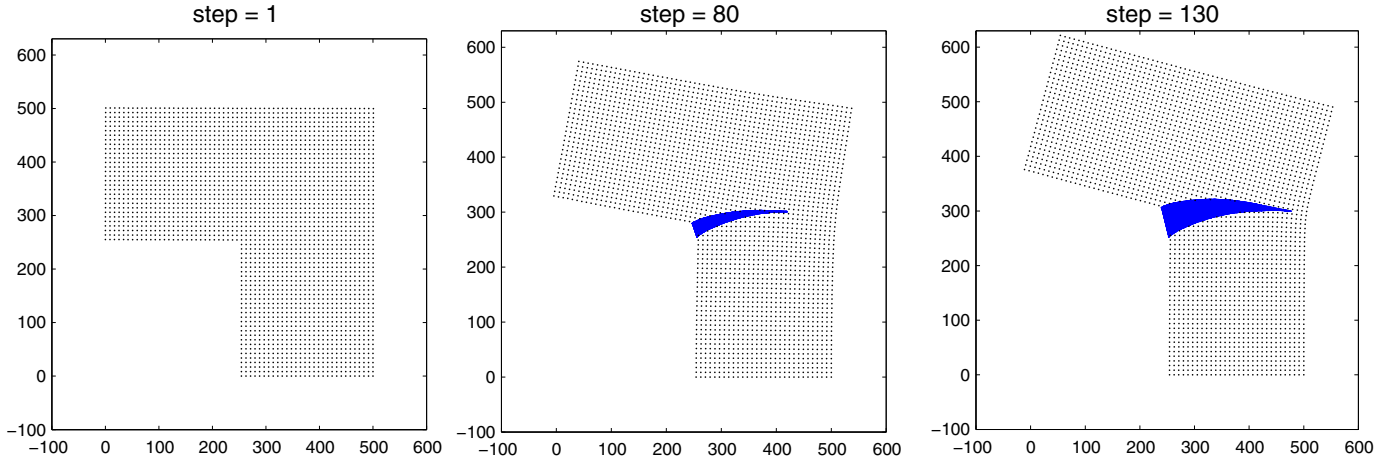

Fig. 23. Deformed mesh (structured) and cohesive zones for the L-shaped panel using the exponential nonlinear cohesive law (magnified by 200×)

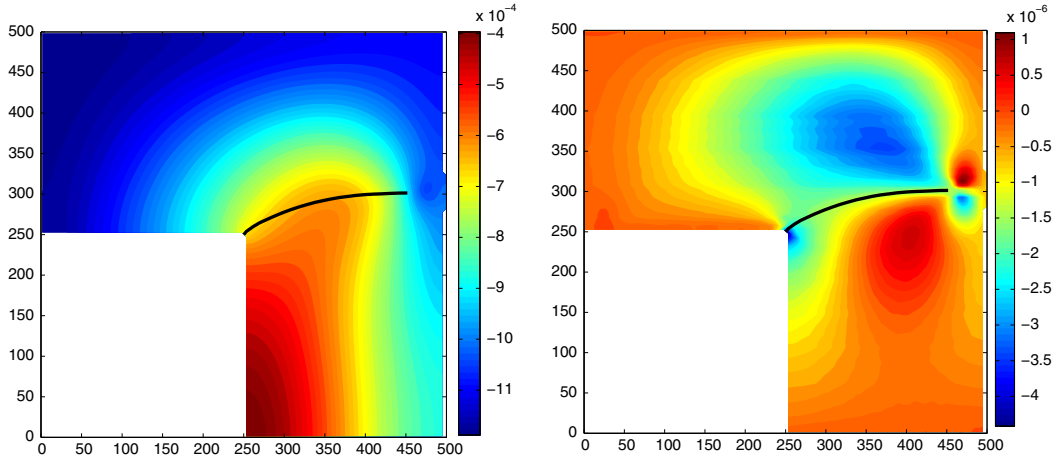

Fig. 24. Water pressure (MPa) (left) and vertical gradient of water pressure (MPa/mm) (right) at the last step of analysis for the problem of mixed mode crack propagation with no mass transfer coupling.

however the differences might not be substantial for the material properties used in the present analysis. It is expected that for smaller values of permeability, this effect can become significant and even lead to convergence difficulties for extremely small values of permeabilities, where high values of water pressure is exerted on the crack surfaces.

4.2.2. Mixed mode crack propagation in saturated porous media – L-shaped panel

For the final numerical example, a mixed mode cohesive crack propagation with a more complex geometry is analyzed. It is selected based on the experiments conducted by Winkler on concrete materials [63] and later assessed numerically by Unger

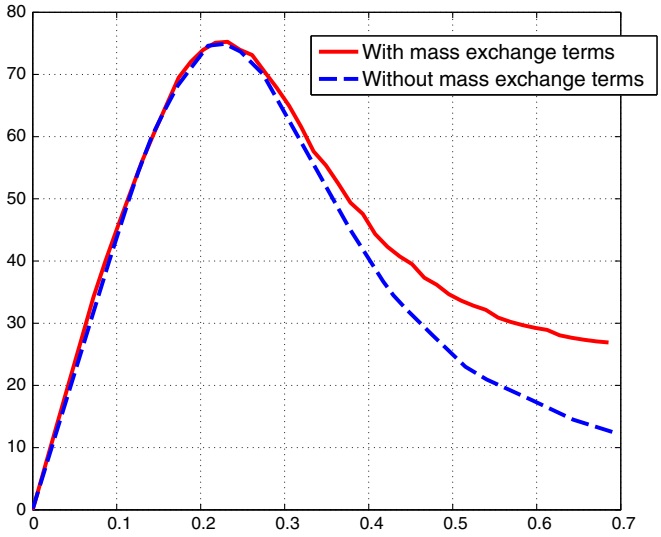

Fig. 25. Load–displacement curve for the L-shaped paned.

et al. [64] and Dumstorff and Meschke [18] using the extended finite element method. An L-shaped panel, shown in Fig. 21, with dimensions of $L = D = 250$ mm and the thickness of 100 mm is considered. The bottom edge is fixed in all directions while prescribed vertical displacements are imposed on a point placed at 30 mm from the left side of the panel, as depicted in Fig. 21. The problem is solved for an increasing prescribed displacement with a constant rate in time. No initial crack is present and it is deemed that the crack nucleates from the corner joint within the panel when the principal tensile stress exceeds the tensile strength of the material. The basic experimental tests by Winkler [63] were performed on dry concrete with no water pressure, but here, the effect of filling water phase in the void volume of the specimen is included. It is assumed that the specimen is totally saturated with water. Then, the boundaries are made impermeable and a displacement control loading is applied until the cohesive fracture is fully developed through the specimen. The basic experimental material properties are $E = 25850$ MPa and $\nu = 0.18$, but in the numerical analysis, Unger et al. [64] proposed to adopt the modified material properties listed in Table 2 in order to match the corresponding experimental load–displacement curves. The value of the time step is taken as 0.1 s. The crack trajectory and the standard and enriched set of nodes along with the imposed boundaries of the problem are shown in Fig. 21.

Fig. 22 shows the load–displacement curves for the case of no fluid coupling along the fracture walls. Similar to [62,64], an exponentially decaying non-linear cohesive law with $f_t = 2.7$ MPa and $G_f = 0.13$ N/mm and $K_p = 25 \times 10^4$ N are used in the present XEFG analysis. A good agreement is observed between the present results and the reference experiments conducted by Winkler [63] and the results reported by Unger et al. [64]. It is noted that these results are produced without considering any coupling term along the fracture line, which confirms that for this case, inclusion of fluid–solid coupling does not change the overall mechanical behavior of the specimen, as similarly reported in [37]. Fig. 23 shows the corresponding deformed configuration in three steps of the crack propagation.

Fig. 24 shows the distribution of water pressure and its vertical gradients at the last step of the analysis, in which the crack is fully developed through the medium. This figure clearly shows that the water pressure distribution is not affected by the discontinuity line in the case that mass coupling is not activated.

To assess the effect of coupling in the analysis, the same problem is solved by considering the full coupling terms, as introduced in Eq. (13). Fig. 25 compares the values resulted from the two cases of analysis, clearly indicating that a higher loading capacity is achieved at the post peak stages of loading in the case of full mass exchange. Fig. 26 displays the contours of water pressure at

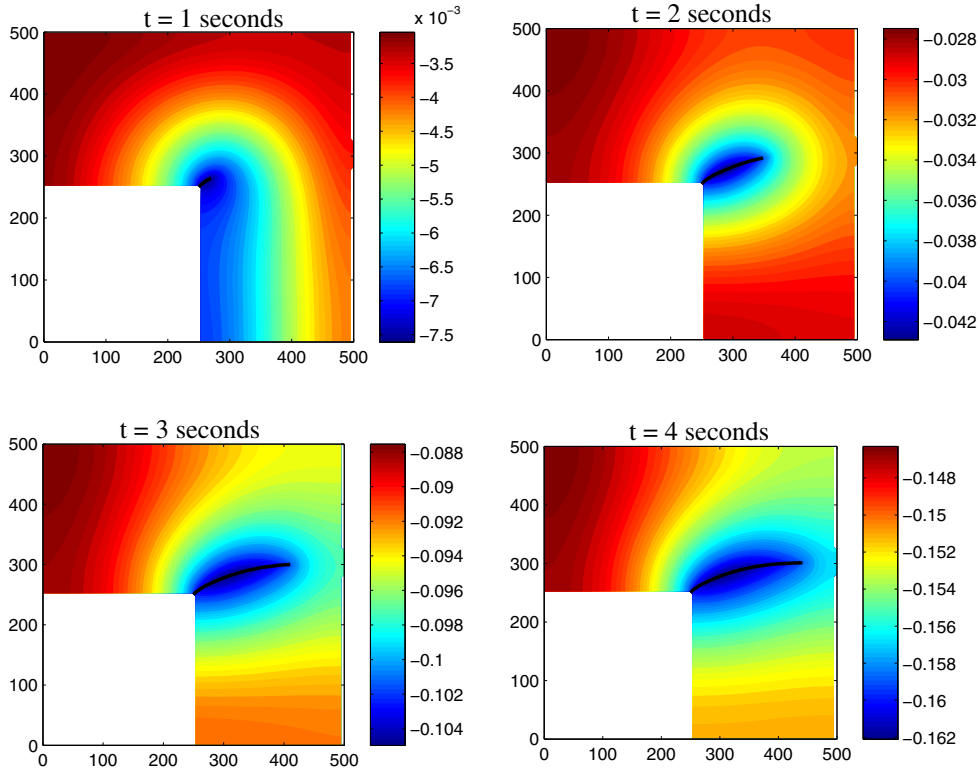

Fig. 26. Water pressure at different times of the analysis for the case of full mass transfer coupling (values in MPa).

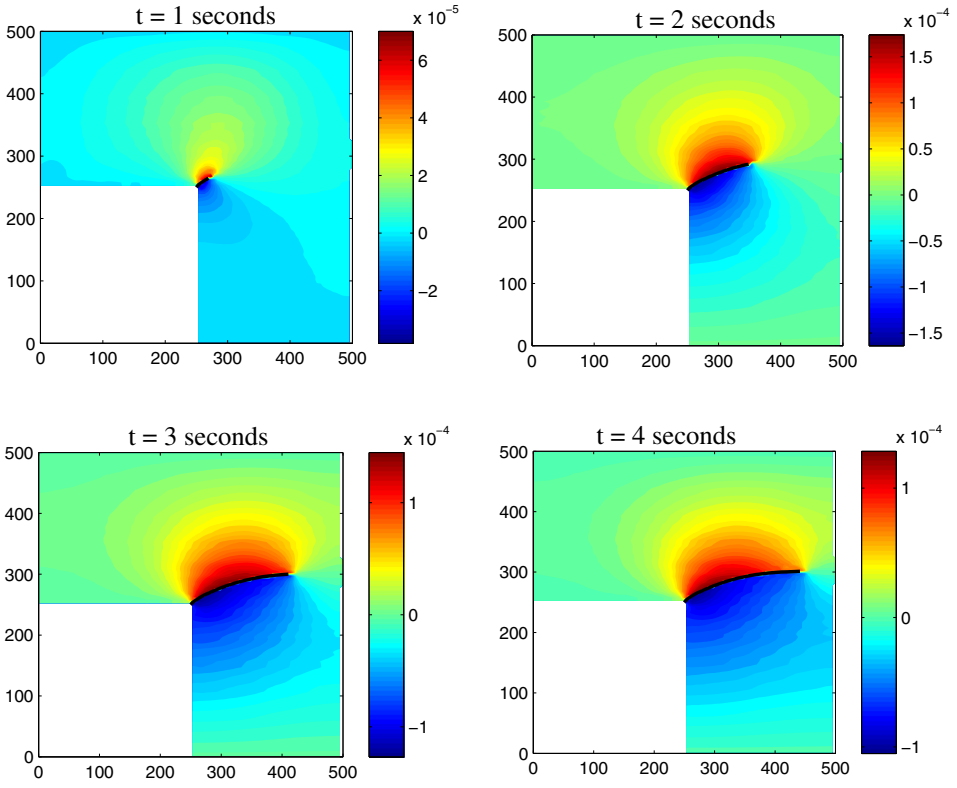

Fig. 27. Vertical gradients of water pressure at different times of the analysis for the case of full mass transfer coupling (values in MPa/mm).

different stages of the analysis, while Fig. 27 shows the corresponding values for the vertical gradient, which becomes discontinuous across the crack surface.

5. Conclusions

In this paper, cohesive crack propagation was assessed through an extrinsically enrichment strategy based on the partition of unity property of MLS shape functions in the context of the element-free Galerkin method. Different problems in single and saturated fully coupled porous media were analyzed by the developed XEFG strategy and good agreement with the reference solutions were reported. Crack lengths were modeled with the Heaviside enrichment functions and the water pressure was enriched with the use of modified distance functions to reproduce discontinuous gradients fields across the crack width. It was observed that neglecting the coupling exchanging terms through the fracture walls would not differ the overall response and the water would flow through the specimen most likely similar to the non-fractured case. However, considering the coupling terms could dramatically change the overall response of the system, both in terms of the mechanical strength and values of water pressure in the media. Problems involving pure mode I and mixed mode fracture in single and fully saturated media considering no couplings and fully coupling along the fracture length were analyzed and the efficiency of the current strategy in handling permeable cohesive cracks were examined.

Conflict of interest

There is no conflict of interest.

Acknowledgements

The authors wish to acknowledge the technical support of the High Performance Computing Lab, University of Tehran. Also, the support of Iran National Science Foundation is gratefully appreciated.

References

[1] Dugdale D. Yielding of steel sheets containing slits. J Mech Phys Solids 1960;8:100–4. http://dx.doi.org/10.1016/0022-5096(60)90013-2.
[2] Barenblatt G. The mathematical theory of equilibrium cracks in brittle fracture. Adv Appl Mech 1962;7:55–129. http://dx.doi.org/10.1016/S0065-2156(08)70121-2.
[3] Hillerborg A, Modeer M, Petersson P-E. Analysis of crack formation and crack growth in concrete by means of fracture mechanics and finite elements. Cem Concr Res 1976;6:773–81. http://dx.doi.org/10.1016/0008-8846(76)90007-7.
[4] Xu X-P, Needleman A. Numerical simulations of fast crack growth in brittle solids. J Mech Phys Solids 1994;42:1397–434. http://dx.doi.org/10.1016/0022-5096(94)90003-5.
[5] Remmers J, Borst R, Verhoosel C, Needleman A. The cohesive band model: a cohesive surface formulation with stress triaxiality. Int J Fract 2013;181:177–88. http://dx.doi.org/10.1007/s10704-013-9834-3.
[6] Carpinteri A, Colombo G. Numerical analysis of catastrophic softening behaviour (snap-back instability). Comput Struct 1989;31:607–36. http://dx.doi.org/10.1016/0045-7949(89)90337-4.
[7] Belytschko T, Black T. Elastic crack growth in finite elements with minimal remeshing. Int J Numer Methods Eng 1999;45:601–20. http://dx.doi.org/10.1002/(SICI)1097-0207(19990620)45:5<601::AID-NME598>3.0.CO;2-S.
[8] Moes N, Dolbow J, Belytschko T. A finite element method for crack growth without remeshing. Int J Numer Methods Eng 1999;46:131–50. http://dx.doi.org/10.1002/(SICI)1097-0207(19990910)46:1<131::AID-NME726>3.0.CO;2-J.
[9] Strouboulis T, Copps K, Babuska I. The generalized finite element method. Comput Methods Appl Mech Eng 2001;190:4081–193. http://dx.doi.org/10.1016/S0045-7825(01)00188-8.
[10] Melenk J, Babuska I. The partition of unity finite element method: basic theory and applications. Comput Methods Appl Mech Eng 1996;139:289–314. http://dx.doi.org/10.1016/S0045-7825(96)01087-0.
[11] Mohammadi S. Extended finite element method. Blackwell; 2007.
[12] Mohammadi S. XFEM fracture analysis of composites. Wiley; 2012.
[13] Zi G, Belytschko T. New crack-tip elements for XFEM and applications to cohesive cracks. Int J Numer Meth Eng 2003;57:2221–40. http://dx.doi.org/10.1002/nme.849.
[14] Bocca P, Carpinteri A, Valente S. Mixed mode fracture of concrete. Int J Solids Struct 1991;27:1139–53. http://dx.doi.org/10.1016/0020-7683(91)90115-V.
[15] Wells GN, Sluys LJ. A new method for modelling cohesive cracks using finite elements. Int J Numer Methods Eng 2001;50:2667–82. http://dx.doi.org/10.1002/nme.143.

[16] Cox JV. An extended finite element method with analytical enrichment for cohesive crack modeling. Int J Numer Methods Eng 2009;78:48–83. http://dx.doi.org/10.1002/nme.2475.
[17] Bocca P, Carpinteri A, Valente S. Size effects in the mixed mode crack propagation: softening and snap-back analysis. Eng Fract Mech 1990;35:159–70. http://dx.doi.org/10.1016/0013-7944(90)90193-K.
[18] Dumstorff P, Meschke G. Crack propagation criteria in the framework of X-FEM-based structural analyses. Int J Numer Anal Methods Geomech 2007;31:239–59. http://dx.doi.org/10.1002/nag.560.
[19] Sukumar N, Chopp D, Mos N, Belytschko T. Modeling holes and inclusions by level sets in the extended finite-element method. Comput Methods Appl Mech Eng 2001;190:6183–200. http://dx.doi.org/10.1016/S0045-7825(01)00215-8.
[20] Chessa J, Wang H, Belytschko T. On the construction of blending elements for local partition of unity enriched finite elements. Int J Numer Methods Eng 2003;57:1015–38. http://dx.doi.org/10.1002/nme.777.
[21] Moes N, Cloirec M, Cartraud P, Remacle J-F. A computational approach to handle complex microstructure geometries. Comput Methods Appl Mech Eng 2003;192:3163–77. http://dx.doi.org/10.1016/S0045-7825(03)00346-3.
[22] Terzaghi K. Theoretical soil mechanics. Wiley; 1943.
[23] Biot MA. General theory of three-dimensional consolidation. J Appl Phys 1941;12:155–64. http://dx.doi.org/10.1063/1.1712886.
[24] Hassanizadeh M, Gray WG. General conservation equations for multi-phase systems: 1. Averaging procedure. Adv Water Resour 1979;2:131–44. http://dx.doi.org/10.1016/0309-1708(79)90025-3.
[25] Hassanizadeh M, Gray WG. General conservation equations for multi-phase systems: 2. Mass, momenta, energy, and entropy equations. Adv Water Resour 1979;2:191–203. http://dx.doi.org/10.1016/0309-1708(79)90035-6.
[26] Lewis R, Schrefler B. The finite element method in the static and dynamic deformation and consolidation of porous media. Wiley; 1998.
[27] Schrefler BA, Xiaoyong Z. A fully coupled model for water flow and airflow in deformable porous media. Water Resour Res 1993;29:155–67. http://dx.doi.org/10.1029/92WR01737.
[28] Schrefler BA, Scotta R. A fully coupled dynamic model for two-phase fluid flow in deformable porous media. Comput Methods Appl Mechods Eng 2001;190:3223–46. http://dx.doi.org/10.1016/S0045-7825(00)00390-X.
[29] Rahman NA, Lewis RW. Finite element modelling of multiphase immiscible flow in deforming porous media for subsurface systems. Comput Geotech 1999;24:41–63. http://dx.doi.org/10.1016/S0266-352X(98)00029-9.
[30] Boone TJ, Ingraffea AR. A numerical procedure for simulation of hydraulically-driven fracture propagation in poroelastic media. Int J Numer Anal Meth Geomech 1990;14:27–47. http://dx.doi.org/10.1002/nag.1610140103.
[31] Schrefler BA, Secchi S, Simoni L. On adaptive refinement techniques in multi-field problems including cohesive fracture. Comput Methods Appl Mech Eng 2006;195:444–61. http://dx.doi.org/10.1016/j.cma.2004.10.014.
[32] Secchi S, Simoni L, Schrefler B. Mesh adaptation and transfer schemes for discrete fracture propagation in porous materials. Int J Numer Anal Meth Geomech 2007;31:331–45. http://dx.doi.org/10.1002/nag.581.
[33] Segura JM, Carol I. Coupled HM analysis using zero-thickness interface elements with double nodes. Part I: Theoretical model. Int J Numer Anal Methods Geomech 2008;32:2083–101. http://dx.doi.org/10.1002/nag.735.
[34] Lobao M, Eve R, Owen D, de Souza Neto A. Modelling of hydro-fracture flow in porous media. Eng Comput 2010;27:129–54. http://dx.doi.org/10.1108/02644401011008568.
[35] Khoei AR, Barani OR, Mofid M. Modeling of dynamic cohesive fracture propagation in porous saturated media. Int J Numer Anal Meth Geomech 2011;35:1160–84. http://dx.doi.org/10.1002/nag.955.
[36] Rethore J, Borst Rd, Abellan M-A. A two-scale approach for fluid flow in fractured porous media. Int J Numer Methods Eng 2007;71:780–800. http://dx.doi.org/10.1002/nme.1962.
[37] Rethore J, Borst R, Abellan M-A. A two-scale model for fluid flow in an unsaturated porous medium with cohesive cracks. Comput Mech 2008;42:227–38. http://dx.doi.org/10.1007/s00466-007-0178-6.
[38] Irzal F, Remmers JJ, Huyghe JM, de Borst R. A large deformation formulation for fluid flow in a progressively fracturing porous material. Comput Methods Appl Mech Eng 2013;256:29–37. http://dx.doi.org/10.1016/j.cma.2012.12.011.
[39] Mohammadnejad T, Khoei AR. Hydro-mechanical modeling of cohesive crack propagation in multiphase porous media using the extended finite element method. Int J Numer Anal Meth Geomech 2013;37:1247–79. http://dx.doi.org/10.1002/nag.2079.
[40] Belytschko T, Krongauz Y, Organ D, Fleming M, Krysl P. Meshless methods: an overview and recent developments. Comput Methods Appl Mech Eng 1996;139:3–47. http://dx.doi.org/10.1016/S0045-7825(96)01078-X.
[41] Liu G. Mesh free methods: moving beyond the finite element method. CRC Press; 2003.
[42] Liu G, Gu Y. An introduction to meshfree methods and their programming. Dordrecht, The Netherlands: Springer; 2005.
[43] Ghorashi SS, Mohammadi S, Sabbagh-Yazdi S-R. Orthotropic enriched element free Galerkin method for fracture analysis of composites. Eng Fract Mech 2011;78:1906–27. http://dx.doi.org/10.1016/j.engfracmech.2011.03.011.
[44] Hua L. Stable element-free Galerkin solution procedures for the coupled soilpore fluid problem. Int J Numer Methods Eng 2011;86:1000–26. http://dx.doi.org/10.1002/nme.3087.
[45] Chen JS, Wu CT, Chi L, Huck F. A mesh-free method for geotechnical materials. J Eng Mech (ASCE) 2001;127:4409.
[46] Wang J, Liu G, Wu Y. A point interpolation method for simulating dissipation process of consolidation. Comput Methods Appl Mech Eng 2001;190:5907–22. http://dx.doi.org/10.1016/S0045-7825(01)00204-3.
[47] Khoshghalb A, Khalili N. A stable meshfree method for fully coupled flow-deformation analysis of saturated porous media. Comput Geotech 2010;37:789–95. http://dx.doi.org/10.1016/j.compgeo.2010.06.005.
[48] Kardani M, Nazem M, Sheng D, Carter J. Large deformation analysis of geomechanics problems by a combined rh-adaptive finite element method. Comput Geotech 2013;49:90–9. http://dx.doi.org/10.1016/j.compgeo.2012.09.013.
[49] Rabczuk T, Zi G. A meshfree method based on the local partition of unity for cohesive cracks. Comput Mech 2007;39:743–60. http://dx.doi.org/10.1007/s00466-006-0067-4.
[50] Irzal F, Remmers JJ, Verhoosel CV, Borst R. Isogeometric finite element analysis of poroelasticity. Int J Numer Anal Meth Geomech 2013;37:1891–907.
[51] Belytschko T, Lu YY, Gu L. Element-free Galerkin methods. Int J Numer Methods Eng 1994;37:229–56. http://dx.doi.org/10.1002/nme.1620370205.
[52] Cordes L, Moran B. Treatment of material discontinuity in the element-free Galerkin method. Comput Methods Appl Mech Eng 1996;139:75–89. http://dx.doi.org/10.1016/S0045-7825(96)01080-8.
[53] Ventura G, Xu JX, Belytschko T. A vector level set method and new discontinuity approximations for crack growth by EFG. Int J Numer Methods Eng 2002;54:923–44. http://dx.doi.org/10.1002/nme.471.
[54] Rabczuk T, Belytschko T. Cracking particles: a simplified meshfree method for arbitrary evolving cracks. Int J Numer Methods Eng 2004;61:2316–43. http://dx.doi.org/10.1002/nme.1151.
[55] Rabczuk T, Areias P. A new approach for modelling slip lines in geological materials with cohesive models. Int J Numer Anal Methods Geomech 2006;30:1159–72. http://dx.doi.org/10.1002/nag.522.
[56] Rabczuk T, Bordas S, Zi G. A three-dimensional meshfree method for continuous multiple-crack initiation, propagation and junction in statics and dynamics. Comput Mech 2007;40:473–95. http://dx.doi.org/10.1007/s00466-006-0122-1.
[57] Rabczuk T, Belytschko T. A three-dimensional large deformation meshfree method for arbitrary evolving cracks. Comput Methods Appl Mech Eng 2007;196:2777–99. http://dx.doi.org/10.1016/j.cma.2006.06.020.
[58] Rabczuk T, Areias PMA, Belytschko T. A simplified mesh-free method for shear bands with cohesive surfaces. Int J Numer Methods Eng 2007;69:993–1021. http://dx.doi.org/10.1002/nme.1797. URL: http://dx.doi.org/10.1002/nme.1797.
[59] Rabczuk T, Areias PMA, Belytschko T. A meshfree thin shell method for non-linear dynamic fracture. Int J Numer Methods Eng 2007;72:524–48. http://dx.doi.org/10.1002/nme.2013. http://dx.doi.org/10.1002/nme.2013.
[60] Goudarzi M, Mohammadi S. Weak discontinuity in porous media: an enriched EFG method for fully coupled layered porous media. Int J Numer Anal Methods Geomech 2014. http://dx.doi.org/10.1002/nag.2281. n/a–n/a. URL: http://dx.doi.org/10.1002/nag.2281.
[61] Moes N, Belytschko T. Extended finite element method for cohesive crack growth. Eng Fract Mech 2002;69:813–33. http://dx.doi.org/10.1016/S0013-7944(01)00128-X.
[62] Zamani A, Gracie R, Reza Eslami M. Cohesive and non-cohesive fracture by higher-order enrichment of XFEM. Int J Numer Methods Eng 2012;90:452–83. http://dx.doi.org/10.1002/nme.3329.
[63] Winkler B. Traglastuntersuchungen von unbewehrten und bewehrten, Betonstrukturen auf der Grundlage eines objektiven Werkstoffgesetzes fur Beton, PhD Thesis, University of Innsbruck; 2001.
[64] Unger JF, Eckardt S, Knke C. Modelling of cohesive crack growth in concrete structures with the extended finite element method. Comput Methods Appl Mech Eng 2007;196:4087–100. http://dx.doi.org/10.1016/j.cma.2007.03.023.